

Diplomarbeit

ILR-RFS DA 21-23

Numerical simulations of Advanced Rocket Nozzles for retro-propulsion in subsonic counter-flows

Carlos Tapia Mancera

Zum
Erlangen des akademischen Grades

DIPLOMINGENIEUR
(Dipl.-Ing.)

Betreuer: M. Sc. Giuseppe Scarlatella
Dipl.-Ing. Martin Propst

Verantwortlicher Hochschullehrer: Prof. Dr. techn. Martin Tajmar

Tag der Einreichung: 19.02.2022

Erster Gutachter: Prof. Dr. techn. Martin Tajmar

Zweiter Gutachter: Dr.-Ing. Christian Bach



Aufgabenstellung für Diplomarbeit

ILR-RFS DA 21-23

Studiengang: Maschinenwesen
Studienrichtung: Luft- und Raumfahrttechnik
Name des Studierenden: **Carlos Tapia Mancera**
Matrikelnummer: 4115339

Thema: Numerische Simulationen von Advanced Rocket Nozzles zur Schuberzeugung in
Unterschall-Gegenströmungen

Subject: Numerical simulations of Advanced Rocket Nozzles for retro-propulsion in subsonic
counter-flows

Motivation:

The "ASCEnSlon" project aims to establish advanced technologies for both ecologically and economically sustainable space access for Europe. The investigation of Advanced Nozzle Concepts (ANCs), such as Aerospike or Dual-Bell, is pivotal in order to advance the TRL of critical technologies for future class of Reusable Launch Vehicles (RLV). A critical aspect is to tailor these novel technologies to recovery strategies, more specifically to vertical landing sustained by propulsion also known as retro-propulsion). In order to develop a numerical and experimental database for ANC with reverse-flow interactions, it is necessary to carry out test campaigns and numerical simulations for different flow regimes. The subsonic test campaign in the vacuum wind channel at TU Dresden and the associated CFD simulations fall under the scope of investigating the landing phase.

Aufgaben:

After a detailed familiarization with the topic and the existing previous work, the following subtasks are to be performed:

- derivation of suitable flow field geometries from the CAD models developed within the research group including a reference conventional bell-nozzle, an annular aerospike nozzle, a dual-bell nozzle (facultative), an Expansion-Deflection nozzle (facultative)
- definition of spatial discretisation in order to perform two-dimensional analyses
- specification of the Boundary Conditions in accordance with the experimental test campaign at ILR utilising subsonic retro-flow (external counter-flow only & counter-flow + main flow), near-vacuum conditions (facultative, main-flow only), sea level conditions (facultative, main-flow only)
- performance of two-dimensional steady state flow simulations and subsequent post-processing of the results, in order to derive the flow-field
- Evaluation of the generated results including but not limited to thrust and drag coefficients and other key parameters of interest (e.g. pressure distribution, distribution of Mach number)
- Verification of selected analyses on the basis of experimental data obtained within the experimental campaign depending on their availability
- refining the CFD models and iterating the simulations in order to increase the fidelity of numerical results (facultative, depending on the outcome of the test campaign)
- submission of complete and comprehensible documentation about the assumptions and decisions made as well as the development process

Rechtliche Bestimmungen:

Der Bearbeiter ist grundsätzlich nicht berechtigt, irgendwelche Arbeits- und Forschungsergebnisse, von denen er bei der Bearbeitung Kenntnis erhält, ohne Genehmigung des Betreuers dritten Personen zugänglich zu machen. Beziiglich erreichter Forschungsleistungen gilt das Gesetz über Urheberrecht und verwendete Schutzrechte (Bundesgesetzbuch I S. 1273, Urheberschutzgesetz vom 09.09.1965). Der Bearbeiter hat das Recht, seine Erkenntnisse zu veröffentlichen, soweit keine Erkenntnisse und Leistungen der betreuenden Institutionen eingeflossen sind. Die von der Studienrichtung erlassenen Richtlinien zur Anfertigung der Studienarbeit sowie die Prüfungsordnung sind zu beachten. Der TUD-Betreuer ist während der Bearbeitung in Form von mindestens 3 Konsultationen über den Status der Arbeit zu informieren. Die „Richtlinien zur Anfertigung von Studienarbeiten“ der Professur, die „Diplomprüfungsordnung“ der Fakultät sowie die „Richtlinien zur Sicherung guter wissenschaftlicher Praxis“ der TU Dresden sind zu beachten.

Betreuer: M.Sc. Giuseppe Scarlatella, ILR, TU Dresden
Dipl.-Ing. Martin Propst, ILR, TU Dresden

Gutachter: Univ.-Prof. Dr. Martin Tajmar, ILR, TU Dresden
Dr.-Ing. Christian Bach, ILR, TU Dresden

Ausgabe: 09.08.2021 **Empfangsbestätigung des Studenten:**
Abgabe: 08.01.2022 Ich bestätige hiermit, dass ich die Aufgabenstellung sowie die rechtlichen Bestimmungen und die Studien- und Prüfungsordnung gelesen und verstanden habe.

Selbständigkeitserklärung

Hiermit erkläre ich, dass ich die von mir beim Institut für Luft- und Raumfahrttechnik der Fakultät Maschinenwesen eingereichte Diplomarbeit zum Thema

”Numerical simulations of Advanced Rocket Nozzles for retro-propulsion in subsonic counter-flows”

selbständig verfasst und keine anderen als die angegebenen Quellen und Hilfsmittel benutzt sowie Zitate kenntlich gemacht habe.

Ort, Datum

Unterschrift

Abstract

Advanced Nozzles Concepts (ANCs) may offer alternative solutions for the future class of Re-usable Launch Vehicles (RLV). Integrating these technologies to RLV can potentially improve the performance of Powered Descent and Landing (PDL) recovery manoeuvres. During the landing burn maneuver, the last stage of a PDL, a vehicle undergoes a phase of sub-sonic retro-propulsion, where the engine is ignited against a low-speed counter-flow.

An aerodynamic and nozzle performance evaluation of a re-usable launcher vehicle during sub-sonic retro-propulsion was made using numerical RANS simulations in ANSYS Fluent. The emerging flow-fields are visualized and values for thrust, specific impulse, and drag are compared between conventional bell and aerospike nozzles. For each nozzle, both designed to have equal thrust at near-vacuum, 4 cases were simulated: on-design static-burn, sea-level static-burn, aerodynamic descent, and sub-sonic retro-propulsion. Initial results confirm a drastic reduction of aerodynamic drag after the activation of the nozzle flow as observed in literature. The simulation results plausibly indicate a distinct higher performance of the aerospike over the conventional bell nozzle (a statement, so far, only valid for these specific designs). The simulations can and should be further optimized and are yet to be validated experimentally.

Contents

Symbol Glossary	V
Acronyms	VII
1 Introduction	1
2 Theoretical Background	3
2.1 Reusable Launch Vehicles	3
2.2 Powered Descent and Landing (PDL)	4
2.2.1 PDL procedure	4
2.2.2 Retro-propulsion: an engineering challenge	7
2.2.3 Sub-sonic Retro-propulsion (SubRP)	9
2.3 Design of Rocket Nozzles	10
2.3.1 The Conventional Bell Nozzle	10
2.3.2 Advanced Nozzle Concepts	12
2.3.3 Rocket Nozzle Design for Retro-Propulsion	18
2.4 Computational Fluid Dynamics (CFD)	18
2.4.1 What is CFD and how does it work?	19
2.4.2 The CFD simulation campaign process	20
2.4.3 Verification, validation, and qualification (VVQ)	22
2.4.4 Turbulence Modelling	24

3 Literature Review	25
3.1 Vertical landing aerodynamics of RLV	25
3.2 Real life vertical landing examples	29
3.3 Supersonic Retro-Propulsion Simulations	31
3.4 Cold flow tests of ANCs in subsonic retroflows	33
4 Methodology	41
5 Problem Definition and Pre-Analysis	45
5.1 Case 1: On-design Static Burn	46
5.2 Case 2: Sea-level Static Burn	48
5.3 Case 3: Aerodynamic Descent	49
5.4 Case 4: Sub-sonic retro-propulsion	52
6 Nozzle Specimen Design	56
6.1 Conventional Bell Nozzle Design	56
6.2 Aerospike Nozzle	58
7 Domain Definition and Discretization	62
7.1 Domain definition	62
7.2 Discretization	64
7.2.1 Mesh: Conventional bell configuration	64
7.2.2 Mesh: Aerospike nozzle configuration	69
8 Simulation Model & Solution Setup	71
8.1 Case 1 Setup	72
8.2 Case 2 Setup	73
8.3 Case 3 Setup	73
8.4 Case 4 Setup	74
9 Results and Post-Processing	75
9.1 Case 1: On-design Static Burn	76
9.1.1 Conventional Bell Nozzle	78
9.1.2 Aerospike nozzle	79
9.2 Case 2: Sea-level Static Burn	80
9.2.1 Conventional Bell Nozzle	81
9.2.2 Aerospike nozzle	82
9.3 Case 3: Aerodynamic Descent	83
9.3.1 Conventional Bell Nozzle	84

9.3.2	Aerospike nozzle	85
9.4	Case 4: Sub-sonic Retro-propulsion	86
9.4.1	Conventional Bell Nozzle	86
9.4.2	Aerospike nozzle	89
10	Verification and Preliminary Validation	91
10.1	Verification	91
10.2	Preliminary validation	92
11	Discussion	94
11.1	Aerodynamic performance	94
11.2	Nozzle performance	95
12	Conclusion and Outlook	97
12.1	Conclusion	97
12.2	Outlook	98
	Bibliography	104

Symbol Glossary

Symbol	Value	Unit	Description
M	-	-	Mach number
p	-	bar	Static pressure
q	-	bar	Dynamic pressure
T	-	K	Temperature
ε	-	-	Expansion ratio
F_x	-	N	Axial thrust
\dot{m}	-	kg/s	Mass flow
A	-	m ²	Area
v, u	-	m/s	Velocity
f	-	N	Momentum flux
Re	-	-	Reynolds number
D	-	mm	Diameter
C_T	-	-	Aerodynamic thrust coefficient
C_{ps}	-	-	Vehicle side pressure coefficient
C_{pb}	-	-	Vehicle base pressure coefficient
NPR	-	-	Nozzle pressure ratio
C_D	-	-	Drag coefficient
H	-	km	Altitude
AR	-	-	Vehicle aspect ratio
ρ	-	kg/m ³	Density
R, R_{air}	287	J/kgK	Specific gas constant (dry air)
g_e	9,81	m/s ²	Earth's gravitational acceleration
γ	1,4	-	Isentropic exponent (dry air)
l	-	mm	length
C_F	-	-	Thrust coefficient
$C_{F_{opt}}$	-	-	Optimum thrust coefficient
r	-	mm	Radius
I_{sp}	-	s	Specific impulse

Symbol	Value	Unit	Description
\dot{w}	-	N/s	Weight flow
d^+	-	mm	Distance from wall to cell center
y^+	-	-	Dimensionless wall distance
n_{lay}	-	-	Inflation layer count
μ	-	Pa s	Dynamic viscosity
k, tke	-	m^2/s^2	Turbulent kinetic energy
ω	-	1/s	Specific dissipation rate
D	-	N	Drag force

Subscript	Description
∞	Freestream
a	Ambient
E	Nozzle Exit
0	Chamber inlet/total
p	Propellant
t	Nozzle throat
j	Jet
ref	Reference/base
v	Vehicle
s	Side
st	Stagnation
b	Base

Acronyms

ANC Advanced Nozzle Concepts

RLV Reusable Launch Vehicle

PDL Powered Descent and Landing

LEO Low Earth Orbit

SRP Supersonic Retro-Propulsion

SubRP Sub-sonic Retro-Propulsion

CD Converging-Diverging

DB Dual-Bell

ED Expansion-Deflection

CFD Computational Fluid Dynamics

FVM Finite Volume Method

CAD Computer Aided Design

2D Two Dimensional

3D Three Dimensional

VVQ Verification, Validation, and Qualification

RANS Reynolds Averaged Navier-Stokes

CFQ Computation of Fluctuating Quantities

LES Large Eddy Simulation

DNS Direct Numerical Simulation

PIV Particle Image Velocimetry

EDL Entry, Descent, and Landing

TUD Technische Universität Dresden

TU Technische Universität

NPR Nozzle Pressure Ratio

o.d. on design

HPC High Performance Computing

TSTO Two-Stage-To-Orbit

RTLS Return To Launch Site

BOS Background-Oriented Schlieren

CHAPTER 1

Introduction

Since the beginning of space exploration, the multistage expendable launch vehicle has been the predominate approach for boosting payloads into orbit. Although this has been a reliable approach, the high cost has limited our endeavors in space [1]. The new class of Re-usable Launch Vehicles has revolutionized the industry, enabling access to space at substantially (20x) lower costs [2].

The most successful method of recovery today is the Powered Descent and Landing (PDL) approach, established commercially by SpaceX. During the recovery procedure, the launcher's first stage undergoes a series of maneuvers, finalizing with a 'landing burn' maneuver. During this maneuver, the vehicle ignites its engine in the direction of flight, against the incoming freestream, to decelerate. This circumstance is called retro-propulsion.

Traditionally, the vehicles use a conventional bell nozzle design for their engines. The role of the nozzle in an engine is to take the heat and pressure generated by the propellant combustion, and convert it into directed impulse to cause a reactive force of thrust (following that for every action there is an equal and opposite reaction; Newton's third law of motion). However advanced nozzle designs have been studied in the past, the aerospike nozzle for example, that can offer up to 20% performance improvement on a launch trajectory [3], allowing the delivery of heavier payloads to farther orbits for the same cost.



Figure 1.1: A Falcon 9 booster finishing its landing burn maneuver, after an ISS resupply mission from 2017. Courtesy of SpaceX

The potential benefits of these advanced nozzles for PDL have not yet been explored. This thesis investigates and compares the performance of the aerospike nozzle against the conventional bell nozzle, during a sub-sonic retro-propulsion maneuver (in the context of the landing burn). Additionally, it contributes an analysis of the aerodynamic behaviour of a vehicle during the same maneuver, leaning on previous experimental work in literature.

After a thorough literature review, the investigation is carried out using Computational Fluid Dynamics (CFD), a numerical simulation method. The simulation models are designed to be comparable with commercial vehicles, and academic literature, but mainly to be compared with a future experimental campaign at the TU Dresden for validation. The simulations are done using a RANS approach for steady state flow using ANSYS Fluent Software. Values for thrust and specific impulse are calculated to assess nozzle performance, and pressure and drag coefficients are calculated to assess the effect of retro-propulsion on the vehicle's aerodynamic performance. The characteristic aerodynamic thrust coefficient is calculated as well. The results offer initial insights and conclusions about the emerging flowfield phenomena and about the aerospike's plausible performance superiority.

CHAPTER 2

Theoretical Background

2.1 Reusable Launch Vehicles

A Reusable Launch Vehicle (RLV) is a technology that enables access to space in a way that the working components (i.e. the rocket engines, fuel and oxidizer tanks, structures, etc.) are not discarded, but effectively recovered and are able to be used again with minimal refurbishment or maintenance. The goal of a RLV is to lower the cost of access to space to promote the creation and delivery of space services to improve economic competitiveness and sustainability [4].

However, the development of a fully (or even just partially) RLV brings many engineering challenges. The recovery of hardware from space requires atmospheric reentry, deceleration, and landing.

Many different recovery methods have been proposed. Reentry can be accomplished either by retro-propulsion, or by utilizing the atmosphere to generate aerodynamic drag [1].

Some methods include the well-known horizontal landing (as performed by the Space Shuttle), parachute & mid-air capture recovery (as planned in by the company Rocket Lab [5]), and the Powered Descent and Landing (PDL) method. In recent years, this last method has been successfully and reliably implemented by SpaceX and their Falcon 9 launcher; revolutionizing the

space sector. Since 2018 SpaceX's Falcon 9 has advertised a cost of \$2,720 per kg to Low Earth Orbit (LEO), compared to the Space Shuttle's cost of \$54,500 per kg. Commercial launch has therefore reduced its cost to LEO by a factor of 20 [2].

Since the success of the Falcon 9 rocket (as of the day of writing, with 71 re-flown launchers), an interest in developing this recovery technology further has been greatly established.

PDL however, is a very payload-expensive attribute for an individual space launch mission. This because the system must carry the fuel required for landing in addition to the fuel already required for the launch. This leads to a strong reduction of usable payload mass capacity or orbital reach [1]. Optimizing this technology is therefore considered worthwhile.

2.2 Powered Descent and Landing (PDL)

Launcher recovery via PDL can be thought of as the reversal of the launch process [1]. The launcher follows a deceleration procedure, reversing its trajectory until it lands vertically, back (or near) to where it started. Depending on the payload mass and the target orbit, the booster may or may not have enough fuel to fly back to the landing zone, and is forced to land elsewhere; on a drone-ship in the middle of the ocean for example.

For example, the recovery of a SpaceX Falcon 9, which is a Two-Stage-To-Orbit (TSTO) launch vehicle, in general follows a four phase procedure after a separation with its second stage. A preparatory phase, a re-entry burn, an aerodynamic descent, and a landing phase. The procedure followed by a Falcon 9 launcher is illustrated in figure 2.1 below.

2.2.1 PDL procedure

A general description of a PDL Return To Launch Site (RTLS) procedure based on a SpaceX Falcon 9 launch mission (NROL-76; [7, 8], see figures 2.2 and 2.3) is as follows.

Firstly, after the stage separation is completed at around 100 km of altitude, the free flying booster performs its preparatory phase. The lack of aerodynamic drag due to the vacuum environment enables efficient maneuvering. The booster flips around (rotation), and corrects its trajectory

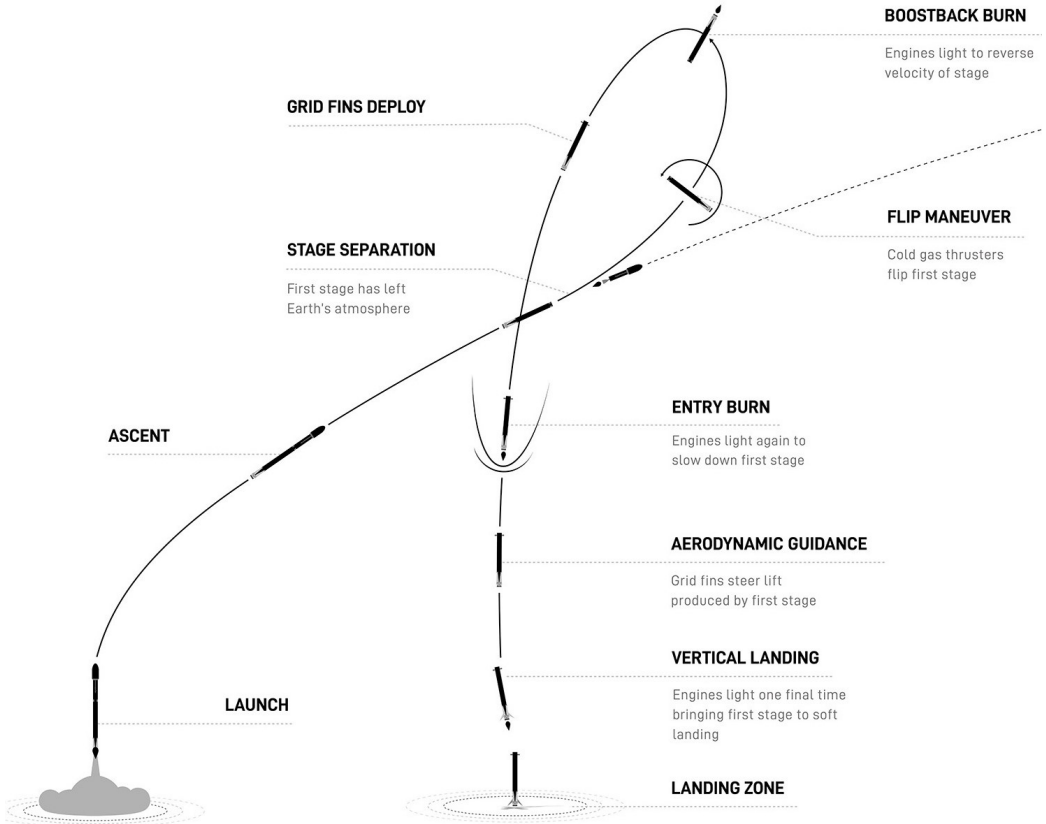


Figure 2.1: A Falcon 9 flight procedure. Modified image, courtesy of SpaceX [6].

(translation) to approach its landing target (the 'Flip' and 'Boostback Burn' maneuver). This prepares the booster for reentry.

Next, the booster implements its deceleration burn (the 'Entry Burn', figure 2.2a) from around 70 km down to 40 km of altitude. This lasts for about 25 seconds. At this phase the booster enters earth's atmosphere and it ignites its engines against the incoming counter flow. The current flight conditions involve hyper-sonic speeds (ca. Mach 5) in near-vacuum pressures (ca. 0,01 bar). This circumstance is called hyper-sonic retro-propulsion. In general, the objective in this phase is to slow down the booster enough, so that it doesn't overheat due to the aerodynamic friction during re-entry.

Next, at around 38 km of altitude ($p_{\infty} \approx 0,04$ bar), the booster per-

forms its aerodynamic descent (figure 2.2b). This lasts around 55 seconds. Here, while being aerodynamically guided to its landing location, most of the booster's accumulated velocity is dissipated aero-thermodynamically through the interaction of its body, its aero-braking and guidance devices (i.e. grid fins) and the atmosphere. The flight conditions involve an increasingly thickening atmosphere, and a transition from hyper-sonic to super-sonic flight, leading to the final phase.

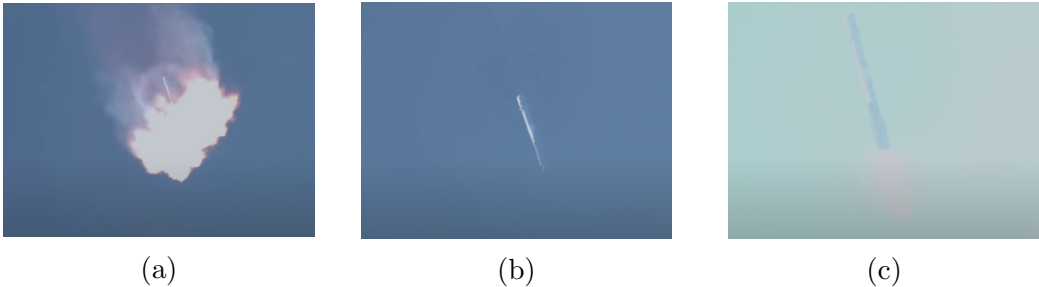


Figure 2.2: The Falcon 9 booster from the mission NROL-76 during its (a) entry burn, (b) aerodynamic descent, and (c) landing burn. Captured from a ground camera, courtesy of SpaceX [8].

The Landing Burn

Finally, at around 4 km of altitude ($p_\infty \approx 0,70$ bar), the landing burn commences. This lasts about 30 seconds. See figures 2.2c and 1.1. The booster's main engine is lit up again for a final burn, pushing its supersonic exhaust plume against an initially super-sonic free-stream counter-flow, then to a sub-sonic counter-flow, until the vehicle's velocity is fully dissipated and the booster smoothly lands on target. This final phase requires the engine to have precise variable throttling to adjust to the decreasing mass of the booster, and the flight conditions involve the highest atmospheric pressures of the flight.

This last phase is highlighted here, since this phase covers the boundary conditions for sub-sonic retro-propulsion and the emerging flow-fields that are studied in the following chapters. An approximation of the landing burn's boundary condition values from start to finish are shown in table 2.1.

Table 2.1: Approximate flight conditions during a landing burn [7].

Variable	Start	End	Unit
Altitude	4	0	km
Pressure	0,7	1,01325	bar
Mach	1,1	0,01	-
Velocity	350	5	m/s
Reynolds no.	$1,2 * 10^8$	$1,9 * 10^6$	-

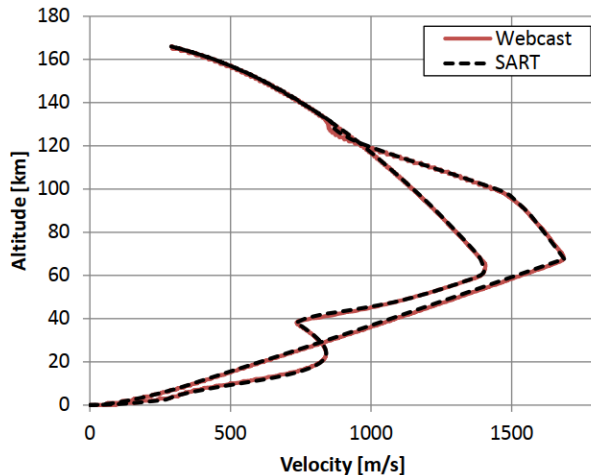


Figure 2.3: Altitude over velocity of a Falcon 9 1st stage during ascent and descent of the NROL-76 mission [8]. The telemetry data (Webcast) and a trajectory model by the German Aerospace Center (SART) are compared. Courtesy of Dumont [7].

2.2.2 Retro-propulsion: an engineering challenge

One of the biggest engineering challenges of a PDL recovery is retro-propulsion. Retro-propulsion is a maneuver where the vehicle is decelerated during atmospheric re-entry, through the firing of one or more engines in the opposite direction of motion [9]. This maneuver is not only relevant for earth re-entry maneuvers, but for atmospheric entry into other planets as well, such as Mars [10]. The main function of this maneuver is to decelerate a spacecraft and

reduce its ballistic coefficient, therefore relaxing its aerodynamic and thermal loads during entry or re-entry.

Retro-propulsion is usually divided in accordance to 3 different flight conditions with decreasing complexity: hyper-sonic ($M > 5$), super-sonic ($M > 1$), and sub-sonic ($M < 1$) flight. Retro-propulsion in sub-sonic conditions, however, is perhaps better known in academia as vertical landing aerodynamics. Each type exhibits different flow-field phenomena and aerodynamic behaviour. In general, the flowfields emerge from the interactions between the vehicle's body, its engine's exhaust plume, and the incoming counter-flow free-stream.

An example of the complex flowfield of a Supersonic Retro-Propulsion (SRP) by Ecker et. al. [11] is shown in figure 2.4.

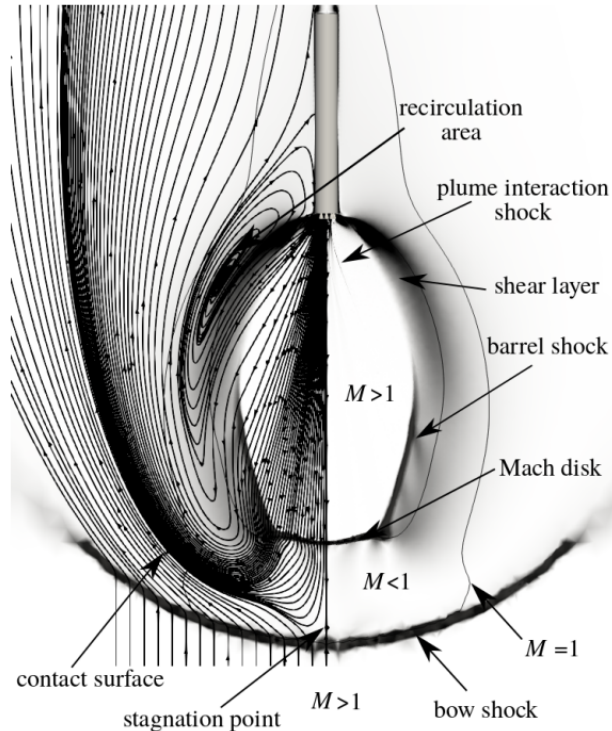


Figure 2.4: SRP flowfield. Courtesy of Ecker [11].

These flowfields are very complex, with strong shock waves, jet-freestream mixing, re-circulation areas, varying sonic conditions, and high turbulence. The phenomena and underlying principles behind this technology are not yet

entirely understood, bringing uncertainties to the design table [12]. Achieving a successful re-entry flight of a RLV requires a thorough investigation of the its aerodynamic characteristics.

A retro-propulsive maneuver is usually characterized by a value called the aerodynamic thrust coefficient ' C_T ' (defined later in section 3.3, eq. 3.4). This value compares the thrust of a vehicle with the strength of the counter-flow, and it usually foretells the features of the flowfield.

An interesting phenomenon for example, depending on the conditions, is that the vehicle may find itself partially submerged in its exhaust plume, as it is pushed downstream by the counter-flow. This can lead to high amounts of heat-fluxes at the lower body portion of the booster, requiring appropriate thermal protection [12].

2.2.3 Sub-sonic Retro-propulsion (SubRP)

The scope of study of this thesis covers only Sub-sonic Retro-Propulsion (SubRP) (closely related to 'vertical landing aerodynamics'), relevant to the landing burn, the final stage of a PDL recovery.

SubRP, in comparison to supersonic and hyper-sonic, is the simplest to analyze, test, and simulate. Its boundary conditions are the most available to recreate in wind-tunnels, its corresponding flow phenomena are relatively better understood, and modern fluid flow computer simulation solvers are better equipped to faithfully model it. This allows for a thorough analysis of at least one part of a PDL recovery and an initial experimentation with new technologies like the ANCs.

SubRP by definition happens in flight conditions where the freestream is below 80% of the speed of sound ($M < 0,8$; from 0,8 to 1,2 it is considered trans-sonic). The vehicle therefore does not create any shock waves upstream. A general observation is that the aerodynamic behaviour of the vehicle drastically changes when the engine is ignited, compared to when it is not. The drag force, for example, reduces dramatically by at least 40% [13].

As later described in the literature review in chapter 3, some experiments and vehicles have already been done on this topic. Where Nonaka et. al. [13] have published a method of study and experimental results, and private companies like SpaceX [8] and Blue Origin [14] have already successfully landed their rockets under comparable circumstances (only at sub-sonic levels). None however, have experimented with different nozzle concepts.

2.3 Design of Rocket Nozzles

Improving the performance of a launch vehicle, both for a launch and a PDL, can be achieved by optimizing its propulsion system. Either by increasing the engine's combustion efficiency, optimizing its combustion cycle, or increasing the efficiency of the nozzle. The latter option can be done with mindful design, and approaching alternative design solutions.

2.3.1 The Conventional Bell Nozzle

As Huzel and Huang [15] explain, "the thrust chamber assembly undeniably embodies the essence of rocket propulsion: the acceleration and ejection of matter, the reaction to which imparts propulsive force to the vehicle. The designer aims to achieve this with a device of maximum performance, stability, durability and minimum size, weight, and cost." The rocket nozzle's task is to transform the released energy from a combustion process, in the form of heat and pressure, into useful kinetic energy [16].

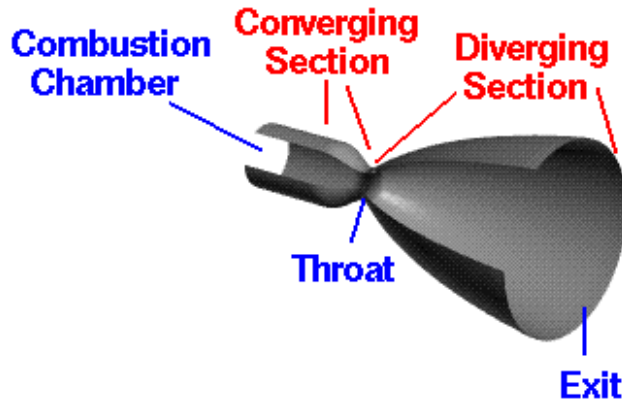


Figure 2.5: Design of a rocket nozzle (a conventional bell). Credit: NASA [17]

As illustrated in figure 2.5, the thrust-chamber body sub-assembly consists of a cylindrical section in which the combustion occurs, a section narrowing toward a throat, and an expanding nozzle section through which the combustion gases are expanded and expelled. This device is also called "De Laval" nozzle, or Converging-Diverging (CD) nozzle.

All the parameters behind the throat being defined, an engineer must then define the geometrical parameters of the expanding nozzle. This depending on the defined combustion chamber conditions (e.g., pressure ' p_0 ', temperature ' T_0 ') and its corresponding ideal expansion ratio ' ε '. An ideal expanding nozzle shape should accelerate the propellant in a uniform direction, while avoiding any losses due to friction, heat dissipation, flow divergence, or internal shock waves.

Conventionally, a bell-shaped expanding nozzle is used. Although this approach has been proven to be reliable and is the current standard [15], it has well-known performance limitations. Namely, it can only perform optimally at its on-design ambient conditions; only at a specific altitude and ambient pressure.

During ascending or descending flight, the vehicle experiences a continuously changing ambient pressure as its altitude changes. This change in ambient pressure directly affects the performance of a nozzle, by adding losses due to flow divergence. The rocket thrust equation 2.1 shown below describes this relationship mathematically. The achievable thrust of a rocket depends on the pressure difference between the nozzle exit and the ambient:

$$F_x = \dot{m}_p \cdot v_E + (p_E - p_a) \cdot A_E \quad (2.1)$$

where

- F_x is the generated axial thrust,
- \dot{m}_p is the mass flow of the propellant gas,
- v_p is the velocity of the propellant gas at the nozzle exit section,
- A_E is the cross-section area at the nozzle exit section,
- and p_E & p_a are the static pressures at the nozzle exit section and the ambient respectively.

The first term ' $\dot{m}_p \cdot v_p$ ' is called the momentum thrust, and the second term ' $(p_E - p_a) \cdot A_E$ ' is called the pressure thrust.

Whenever there exists a difference between the pressures in the second term, the nozzle will under-perform and therefore lose efficiency. When the ambient pressure is higher than the pressure of the flow at the nozzle's exit,

the flow is said to be *over-expanded*. When it's lower, it is *under-expanded*, and when both pressures match, the flow is *optimally expanded*. Figure 2.6 illustrates this phenomenon. The loss in thrust comes partly from the fact, that part of the flow diverges; i.o.w. it is expelled in the 'wrong' (non-axial) direction, failing to contribute to the reaction force in the desired direction of thrust. Additionally, if the flow separates from the wall before the exit, the nozzle fails to use its full expansion capability, resulting in a lower exhaust velocity.

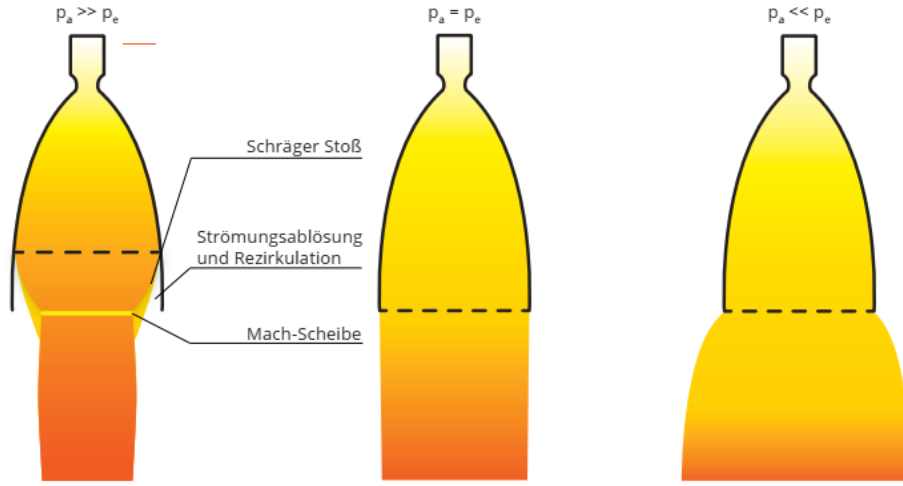


Figure 2.6: An over-expanded, an optimally expanded, and an under-expanded nozzle flow. Courtesy of Dr. Bach [18]

Considering this, a nozzle is usually optimized for a specific altitude and its corresponding ambient pressure. The selected design altitude attempts to find a compromise between high efficiency in a wide altitude range and an ensured attached and stable flow at the starting altitude and ignition. According to Huzel and Huang, traditional first stage boosters, which spend most of their flight within the atmosphere, are usually optimized at around $p_a = 0,4$ bar or 70 km of altitude, while second stages are optimized at near-vacuum for in-space conditions [15].

2.3.2 Advanced Nozzle Concepts

Advanced rocket nozzles or Advanced Nozzle Concepts (ANCs) are design solutions that promise a gain in performance over existing conventional no-

zles. For example, according to Hagemann et. al [3], significant performance gains result from the adaptation of the exhaust flow to the changing ambient pressure. This kind of ANC s are called altitude-adaptive nozzles and they could theoretically overcome performance losses up to 15% during the ascent phase, compared to the conventional bell-nozzle adapted to sea-level operations [3].

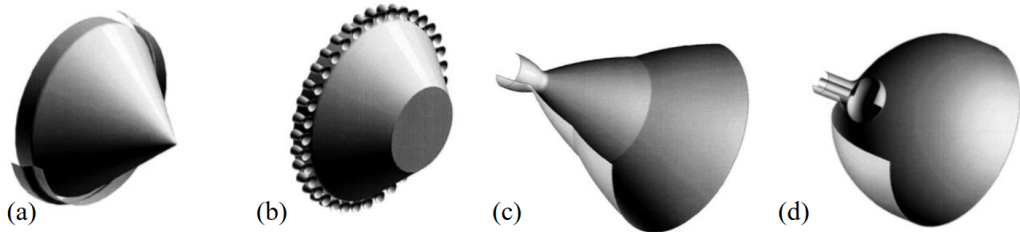


Figure 2.7: ANC models: (a) annular aerospike, (b) annular-truncated clustered aerospike, (c) dual-bell and (d) expansion-deflection nozzles. Modified image from Hagemann et. al [3].

For this reason, several altitude-adaptive ANC s have been proposed, each with their own special characteristics. The annular aerospike, the dual-bell, and the expansion-deflection nozzles are briefly described in the following paragraphs.

The Dual-Bell Nozzle (DB Nozzle)

The Dual-Bell (DB) Nozzle, see figure 2.7 (c), offers a one-step discrete (discontinuous) passive altitude adaptation without any moving parts. This is done by nozzle wall-inflection; the nozzle wall is slightly bent outwards at a point where a fixed nozzle extension begins.

This configuration controls the nozzle flow by ensuring flow separation at the inflection point when working in lower altitudes. This creates a lower effective expansion ratio. After the design altitude of the first nozzle section is reached, the flow transitions and attaches to the second section using the full expansion capability of the nozzle. See figure 2.8. In short, this design offers the following highlighted advantages and disadvantages [18] shown in table 2.2:

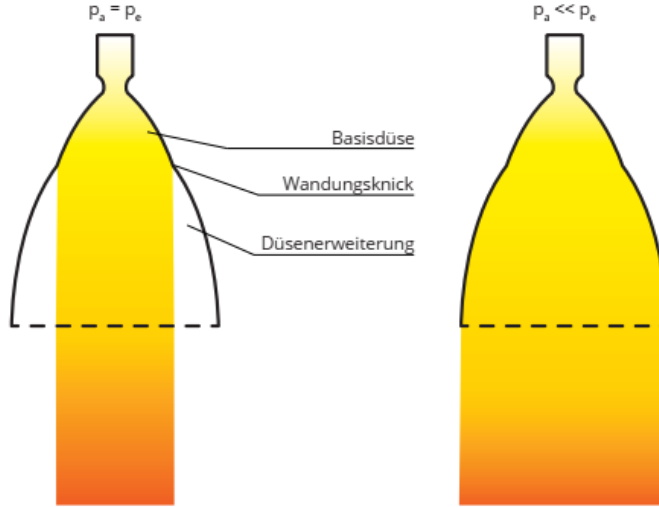


Figure 2.8: The two flow states in a dual-bell nozzle. Flow separation at the wall-inflection (left), and full flow along the extension (right). Courtesy of Dr. Bach [18]

Table 2.2: Advantages and disadvantages of Dual-Bell nozzles [18]

Advantages	Disadvantages
Simple geometry	High thermo-mechanical loads near the wall-inflection
High reliability, no moving parts needed	Higher mass and volume
Good altitude-adaptive qualities	Operation considerations must be made to optimize the transition from detached flow to attached flow
Relatively simple implementation	At vacuum conditions, the inflection at the wall adds efficiency losses

The Expansion-Deflection Nozzle (ED Nozzle)

An Expansion-Deflection (ED) nozzle, shown in figure 2.7 (d) and figure 2.9, expands its exhaust gas adapting passively and continuously to the ambient

pressure. The expansion process adapts inside of the nozzle, in contrast to the following aerospike nozzle.

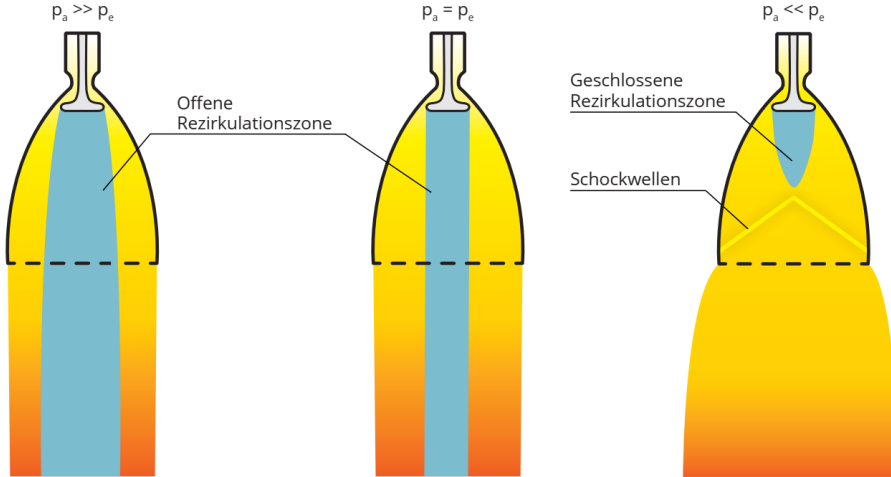


Figure 2.9: The three flow states in an expansion-deflection nozzle. Over-expansion (left), optimal expansion (middle), and under-expansion (right). Courtesy of Dr. Bach [18]

This is done by diverting the exhaust flow from the nozzle's throat with a central body placed nearby. The deflected exhaust gas is then accelerated and redirected along the nozzle walls, through a series of re-compression shocks and expansion waves. A wake then forms in the center of which boundaries are driven by the ambient pressure. This allows for the design's passive flow expansion regulation [19]. Some advantages and disadvantages [18] are shown in table 2.3.

Table 2.3: Advantages and disadvantages of ED nozzles [18]

Advantages	Disadvantages
Higher efficiencies compared to bell nozzles	Difficult cooling of the central deflecting body.
Better performance in vacuum than dual-bell nozzles due to its compactness.	Complex flow field
High flow stability over a large altitude range	The efficiency of the nozzle fluctuates significantly in function of the pressure ratio
	Complex shape

Comparing the ED nozzle with the DB nozzle, one can make some general remarks. DB nozzles perform better at lower pressure ratios, while ED nozzles do better at higher pressure ratios. Moreover, DB design is simpler, while the complexity of ED makes it hard to assemble and maintain.

The Aerospike Nozzle

Aerospike nozzles offer passive and continuous altitude adaptation up to their geometrical area ratio. A distinction is made between annular and linear designs, and designs where there is one or a cluster of combustion chambers before the throat. Figures 2.7 (a) and (b) illustrate these designs and figure 2.10 describes its function under its 3 different states. Additionally, as an effort to relieve manufacturing and thermal management constraints, the central 'spike' body is usually truncated to a certain spike length percent.

While conventional bell nozzles expand the gas along their fixed outer contour, the central 'spike' body of an aerospike nozzle allows the exhaust gas to continuously expand along a physical central spike and the aerodynamic boundary according to the ambient pressure, while ensuring a congruent exhaust flow direction.

Aerospike nozzles have the following significant advantages and disadvantages [18] shown in table 2.4:

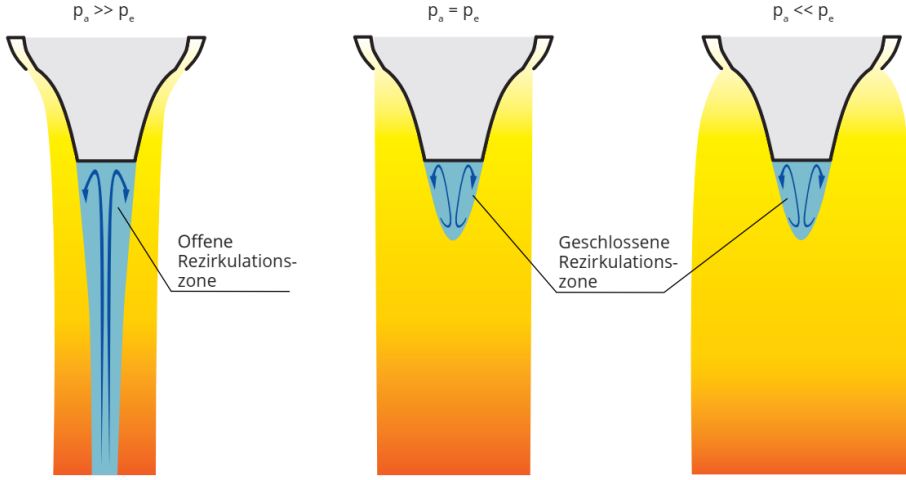


Figure 2.10: The three flow states on a truncated aerospike nozzle. Over-expansion (left), optimal expansion (middle), and under-expansion (right). Courtesy of Dr. Bach [18]

Table 2.4: Advantages and disadvantages of Aerospike nozzles [18]

Advantages	Disadvantages
Significantly higher thrust efficiency and specific impulse at low altitudes compared to bell nozzles.	High thermal management challenges, due to significantly higher areas with a high heat flux (i.e. the long annular throat).
Higher thrust performance in vacuum than bell nozzles due to higher allowed expansion ratios.	Difficult manufacturing challenges.
Over-expanded flow portions are course corrected more effectively than in bell nozzles. This potentially gains a 5% thrust increment.	Very complex design; complex combustion chambers. Low technology readiness level.
Smaller, more compact design.	Difficult thrust vector control.
	No altitude adaptation beyond its design point.

Despite its complexity, aerospike nozzles have a lot of potential. And due

to recent innovations in manufacturing capabilities through additive manufacturing, its feasibility is increasingly promising [18].

2.3.3 Rocket Nozzle Design for Retro-Propulsion

While the design of ANCs for ascension has been thoroughly explored in academia (for example by the work of Hagemann et al. [3]), exploring the benefits of tailoring these nozzles for PDL recovery and retro-propulsion has not yet been done [20]. Taking advantage of ANCs altitude-compensating capabilities for entry-burn and landing burn maneuvers may overall increase the propulsive performance along the descension trajectory, leading to further payload and range gains for the overall mission.

In a market sector, the space launch sector, constantly pushed by private companies towards innovation and competitiveness, using ANCs for launch vehicle recovery could offer a disruptive technology worth developing [20].

2.4 Computational Fluid Dynamics (CFD)

Historically, aerodynamicists and aeronautical engineers have solved fluid flow problems with the means of experimentation and mathematical analysis. These two approaches are indeed effective for a remarkably wide range of fluid flow problems. However, in the last century fluid flow problems have increased in complexity so much that engineers have reached the limits of the state of the art of aerodynamic theory, having to resort to a new approach.

A canonical example of such a complex flow is the flow around a vehicle in re-entry, such as a ballistic missile or a space shuttle (or a Re-usable Launch Vehicle). This because the flowfield involves sub-sonic flow as well as super-sonic flow and viscous flow. Although analytical techniques exist to tackle each of these kind of flows separately to a certain extent, a universal technique that blends them all does not yet exist [21]. Additionally, experimentation of such complex flows needs increasingly expensive equipment and clever test setups to gather any useful data.

The advent of the computer and its exponentially increasing computing power at a decreasing cost in the last decades has enabled a new approach to solve complex fluid flow problems: Computational Fluid Dynamics (CFD). CFD allowed engineers in the 1960's to find a practical solution to the design of a re-entry vehicle for the first time. Since then CFD revolutionized aero-

dynamics and is now considered the third dimension in fluid flow analysis, in addition to experimentation and analytical theory [21].

Today engineers, with the foundation of analytical theory, use CFD for the design of aircraft and spacecraft (amongst many other things) as a way to test the preliminary designs, only using experimentation (i.e. wind tunnel testing) as a way to fine-tune and validate their designs.

However, CFD presents its own limitations as well. To make any use from CFD, an engineer must be able to gauge the accuracy of the chosen mathematical models (facing the problem of modelling turbulent flow), while considering the intrinsic computational errors (i.e. round-off, linearization, and discretization errors), without setting up a numerical procedure that takes too long to solve. An engineer using CFD must therefore find the compromise between accuracy (how faithfully the physics are modelled), numerical certainty (how well the mathematical model is solved), and computational cost (in terms of computational time and equipment for example).

2.4.1 What is CFD and how does it work?

Fluid dynamics is governed by the principle of conservation applied to the mass, energy, and momentum of a given system with defined boundaries; i.e. a volume closed and constrained by a surface. These principles can be expressed in terms of mathematical equations (either partial differential equations PDEs or integral equations). Computational fluid dynamics (CFD), as a numerical method, is the art of replacing the governing mathematical equations of fluid flow with numbers, and advancing these numbers in space and/or time to obtain a numerical description of the complete flow of interest [21].

CFD uses the Finite Volume Method (FVM), a numerical method that discretizes the integral form of the conservation equations. In this method a flow-field is subdivided into a set of non-overlapping cells that cover the whole domain. The conservation laws are applied to determine the flow variables within the cells in relation to its neighboring cells and/or boundary conditions [22].

Starting with an initial guess (initialization), the flow variables for each cell are determined through an iterative process, where each new iteration attempts to adjust the cell variables in a way that reduces any numerical residue that would constitute to a violation of the conservation laws (any missing or excess energy, momentum, or mass between cells and within the

whole domain).

The process however is never perfect, and a certain amount of numerical residue is tolerated. When the residual values sink with each iteration in a stable way below the tolerance level (carefully defined by the engineer), numerical convergence is achieved (at least partially). Further convergence is assessed by monitoring the behaviour of additional selected values throughout the iterative process. In contrast, diverging residuals or monitored values that never sink or that even keep increasing and/or behave in an unstable way, indicate a faulty simulation setup that provides unreliable and/or nonphysical results.

Finally, when the solution is deemed sufficiently convergent, the cell variable values are conclusively resolved, and quantitative data can be extracted and plotted for further analysis.

2.4.2 The CFD simulation campaign process

In practice, a CFD numerical simulation campaign usually follows this ten step process [23, 24, 25]:

1. **Problem specification:** the physical problem is specified in detail. The relevant physics, the given working fluid, its boundary conditions (i.e. pressure, velocity, temperature) as well as the spatial and time domain are defined. Additionally, the resulting physical values and fields of interest such as drag, velocity contours and vectors, and pressure contours, are also defined.
2. **Pre-analysis:** a preliminary analysis of the problem is made using any available experimental data and analytical theory (or hand calculations). This has the intention of acquiring a faithful prediction of the topology and characteristics of the flow field in investigation. This is used as a hint or a reference to prepare the simulations accordingly and assess the validity of the simulation results throughout the campaign.
3. **Domain definition:** a derivation of a suitable flow field domain geometry is made (2D, 3D, axis-symmetric, etc.). This is usually done in detail with a Computer Aided Design (CAD) package.
4. **Domain discretization (meshing):** the domain is subdivided in a finite quantity of volumes (called cells) adapting its granularity to any

areas of considerable interest and detail (i.e. boundary layers or shock waves). The final result of this discretization is a mesh. A helpful analogy for this is the resolution of an image in a screen, where the amount of pixels, their size and distribution determines how sharply the details in the image are resolved. A mesh typically contains from thousands of cells for simple flowfields, up to billions of cells for high definition complex flowfields. More cells result in a higher computational cost. A good mesh provides sufficient resolution, enables numerical convergence, and minimizes the cell count to reduce computational cost [26].

5. **Numerical model setup:** a mathematical model of the physics is chosen depending on the expected characteristics of the flow. Depending on the type of flow and the given assumptions (i.e. incompressible or compressible, laminar or turbulent, 2D or 3D, steady or unsteady, etc.) one may or may not need to include certain models such as the energy and turbulence equations. Simpler models relax the computational cost and tend to be easier to converge, but sometimes at the cost of diminished accuracy. It is therefore important to understand that CFD solutions are bound to the degree of physics that goes into their formulation [21].
6. **Application of the boundary conditions:** the physical conditions on every boundary surface of the domain (i.e. inlets, outlets, and walls) are defined. Typically boundary types like pressure inlets, velocity inlets, no-slip walls, and pressure far-fields are used, where the flow variables are (mostly) independent from the rest of the domain.
7. **Solution setup:** in this step, the settings for solving the chosen mathematical model, "under the hood" or "inside the blackbox", are defined in order to control the numerical stability and convergence of the solution process. Though modern commercial simulation packages are usually equipped to assume most of this task, sometimes a user must intervene and adjust accordingly to optimize a desired algorithm or a solution technique [24].
8. **Results (post-processing):** After the solution sufficiently converges, the flow-field data can be easily manipulated and presented in the form of colour contours, plots, and animations for its easier understanding and in-depth analysis.

9. **Verification and validation:** The accuracy and reliability of the computational simulation is assessed through the process of verification and validation. The former serves to assess simulation *numerical* uncertainty (how well the mathematical model was solved) analyzing the numerical process, while the latter assesses simulation *model* uncertainty (how well the mathematical model represents nature) comparing the numerical results with experimental data [25, 27].
10. **Qualification:** Though it is not formally acknowledged in popular simulation practices, this final step of qualification serves to assess if the computational model is in sufficient agreement with reality for it to bring value to the specific practical application at hand [25]. These last two steps are covered in more depth on section 2.4.3.

Furthermore, a numerical simulation is rarely qualified in the first attempt. Diverging residuals and unstable numerical behaviour are common. Therefore the engineer must keep improving the simulation setup, iterating through this nine step process until the simulation setup is optimized and valuable data can be extracted.

According to CFD communities, the recommended simulation practice is to start with a simplified version of the problem at hand, modelling to ensure convergence to then collect hints about the topology of the complex flowfield. Then carefully increase the complexity with each simulation building up from the previous ones, up to the final sufficiently complex flow-field.

2.4.3 Verification, validation, and qualification (VVQ)

The last steps in a numerical simulation campaign is the Verification, Validation, and Qualification (VVQ). These are the primary ways to assess the accuracy and reliability of a computational simulation, and its applicability to the given problem. In literature these terms are often confused, reflecting their definition's ambiguity. This thesis uses the definitions discussed by Oberkampf and Trucano [25] summarized in the next paragraphs, while in figure 2.11 a schematic shows the relation between reality, the computerized model, and the conceptual model.

Verification is the assessment of the accuracy of the solution to a computational model by a comparison with known solutions. It is primarily a mathematics issue. Its objective is to identify and quantify errors and uncertainties in the computational model and its solution. It provides evidence

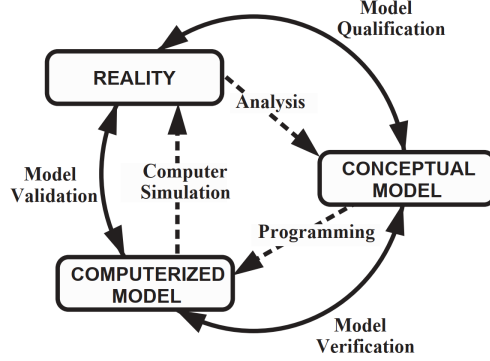


Figure 2.11: The phases of modeling and simulation and the role of VVQ [25]

that the conceptual model is solved correctly, but it doesn't address whether it has any relationship to the real world [25]. For instance, analyzing the sign and magnitude of a numerical error and the convergence conditions of certain values (monotonic, oscillatory, or divergent) can provide this evidence. (e.g. in a rocket nozzle flow, does the resulting thrust value converge monotonically over many iterations? With what magnitude of residuals?)

Validation, on the other hand, is the process of determining the degree to which a model is an accurate representation of the real world. It provides evidence for how accurate the computational/conceptual model simulates reality, assuming it was previously verified. Fundamentally, validation asks how formal constructs of nature (mathematical models) can be tested by physical observation. Practically speaking, it assesses how accurately the computational results compare with experimental data, with quantified error and uncertainty estimates for both [25]. (E.g. in a rocket nozzle flow, in percentage, how close does the calculated thrust match the measured thrust?)

Finally, qualification determines the adequacy of the computational/conceptual model to provide an acceptable level of agreement for the domain of intended application based on a defined requirement. Basically, it judges whether the quantified error and uncertainty is small enough for the simulation to be useful for the given application [25, 28]. (e.g. in a rocket nozzle flow, does the calculated value of the thrust match the measured thrust above a requirement of say 95%?)

2.4.4 Turbulence Modelling

A particular challenge in CFD simulations is that of turbulence modelling. This plays a role during the numerical model setup (step 5 of section 2.4.2) and it has a severe influence in a simulation's both numerical and model uncertainties. Most CFD solutions of turbulent flows now contain turbulence models which are just approximations of the real physics, and depend on experimental data to adjust various constants within their mathematical model. Turbulent flows (characterized by unsteady, irregular, seemingly random and chaotic motion) are especially difficult to model and are therefore particularly subject for error. Consequently, the CFD community is directly attacking this problem; Turbulence modelling is currently a wide-open area of research with a lot of activity [21]. For example, modern approaches involve innovative machine learning algorithms [29].

In practice many models are available for use in commercial simulation packages, where the user must choose, with engineering judgement, the most appropriate model for the flow-field at hand. In general, they are classified in two main areas: Reynolds Averaged Navier-Stokes (RANS) models, and Computation of Fluctuating Quantities (CFQ) [30].

In the RANS models, (such as the "k- ϵ ", "k- ω ", "k- ω -SST", or "Spalart-Allmaras" models) the fluctuating unsteady behaviour of the turbulent flow field is averaged out into steady mean values. This allows for lower computational costs, while maintaining a meaningful physical behaviour. The particular models vary on the assumptions made, the techniques implemented, and the experimental data they are based on; some offering better accuracy and/or convergence for certain types of flow-fields than others.

On the other hand, in the CFQ (such as the Large Eddy Simulation (LES), or Direct Numerical Simulation (DNS)) the approach is direct. LES directly computes the time-varying flow down to a certain resolution, only modelling the unsteady flow below this specified resolution. While DNS does no modelling whatsoever and is required to resolve the unsteady flow down to the smallest scales. Both of these, but especially DNS, require very high computational resources.

CHAPTER 3

Literature Review

Some research and development on sub-sonic retro-propulsion has been documented in academic literature and in the private sector, and some even with the use of ANCs. Academic experimental research on vertical landing aerodynamics, some documented numerical simulations, as well as real life examples of vehicles performing landing burn maneuvers already provide valuable data and an initial path of study. Additionally, a test campaign from the Technische Universität Dresden (TUD) provides the experimental dimension to the study.

3.1 Vertical landing aerodynamics of RLV

The work of Nonaka et al. on *Vertical Landing Aerodynamics of Reusable Rocket Vehicle* [13] provides a methodology to study the aerodynamic performance of a landing vehicle, as well as conclusive results and flowfield data from experimental results.

In his experiment, a scaled model of a re-entry vehicle is put inside a wind tunnel. The vehicle has an aeroshell shape with a built-in cold-gas rocket nozzle (conventional bell; $A_t = 3,14 \text{ mm}^2$, $A_E = 7,07 \text{ mm}^2$) on its base along the axis. The wind tunnel provides a counter-flowing freestream which parameters correspond to flight conditions as defined in table 3.1.

Aerodynamic forces and surface pressures are measured and flow topologies are visualized using Particle Image Velocimetry (PIV).

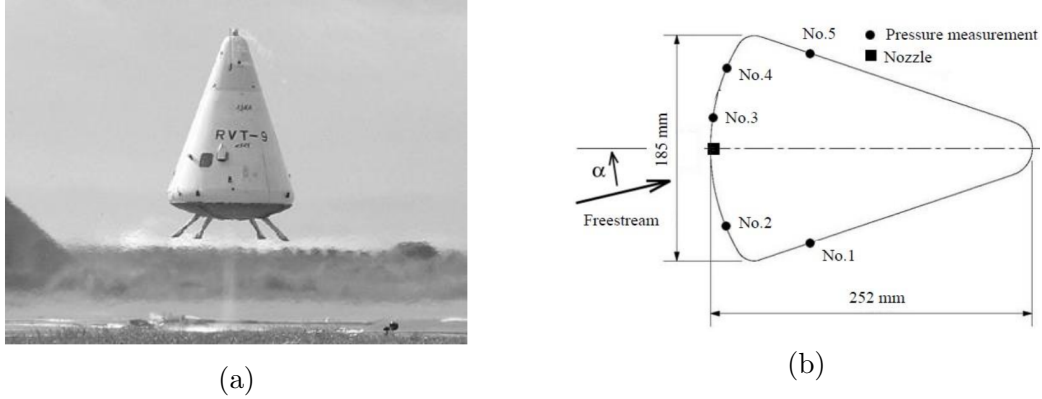


Figure 3.1: Nonaka's et al. vehicle (a) and its sub-scaled model schematic (b) [13].

Table 3.1: Nonaka's vehicle flight and test conditions [13].

	Vehicle Flight	Wind tunnel test
T_0 [K]	3415	289
p_0 [bar]	24,3	20,8
p_a [bar]	1,019	1,015
u_∞ [m/s]	70	26,4
M_j	2,41	2,41
Re_∞	$3,5e^5$	$3,5e^5$
Re_j	$5e^6$	$5e^6$
p_E/p_a	1,38	1,38
f_j/f_∞	0,769	0,769
D_E/D_{ref}	61	61

Various thrust level cases are studied, including a case with null thrust (jet off). Their results are shown in figure 3.2 and table 3.2. Some key takeaways are:

1. The comprehensive structure of the jet/freestream interaction is dominated by the **momentum flux ratio** ' f_j/f_∞ ' of the freestream against

the counter jet , where

$$f_j = \rho_j u_j^2 \cdot A_E \quad (3.1)$$

is the momentum flux of the jet defined by the nozzle's exit cross section area and

$$f_\infty = \rho_\infty u_\infty^2 \cdot A_{ref} \quad (3.2)$$

is the momentum flux of the freestream, defined by the base area. This value is comparable to the ***aerodynamic thrust coefficient*** ' C_T ' (eq. 3.4) in the context of retro-propulsion defined later in section 3.3. A key difference is that the momentum flux ratio only considers that: the momentum fluxes, while the ' C_T ' considers all components of thrust.

$$C_T \neq f_j/f_\infty \quad (3.3)$$

2. A drastic reduction of the aerodynamic drag (down by 76%) is observed when the exhaust jet is on.
3. Pressure increases by 40% on the side body surface and decreases by 58% on the base surface when the exhaust jet is on.
4. While there is flow separation when the jet is off, the flow reattaches when turned on (when at max.).
5. The pressure ratio $p_E/p_a = 1,38$ implies an under-expanded nozzle flow.
6. A re-circulation area emerges upstream after the stagnation point, where the jet encounters the freestream. The distance of this stagnation point is correlated to the aerodynamic thrust coefficient, where lower values can imply a stagnation point closer to the body.

Table 3.2: A sample of Nonaka's test results [13]. Cases: zero thrust (Jet off) and maximum thrust (Jet on). *Originally not included, estimated by the author.

Parameter	Symbol	Jet off	Jet on	Unit
Thrust	F_x	0	8,93	N
Chamber pressure	p_0	0	20,8	bar
Freestream velocity	u_∞	26,4	26,4	m/s
Nozzle pressure ratio	$NPR = p_0/p_a$	0	20,49	-
Nozzle exit to ambient pressure ratio	p_E/p_a	0	1,38	-
Momentum flux ratio	f_j/f_∞	0	0,769	-
Aero. thrust coefficient*	C_T	0	1,54	-
Pressure coefficient at the base	C_{pb}	0,95	0,4 (-58%)	-
Pressure coefficient at the sides	C_{ps}	-0,38	-0,15 (+40%)	-
Drag coefficient	C_d	0,75	0,18 (-76%)	-

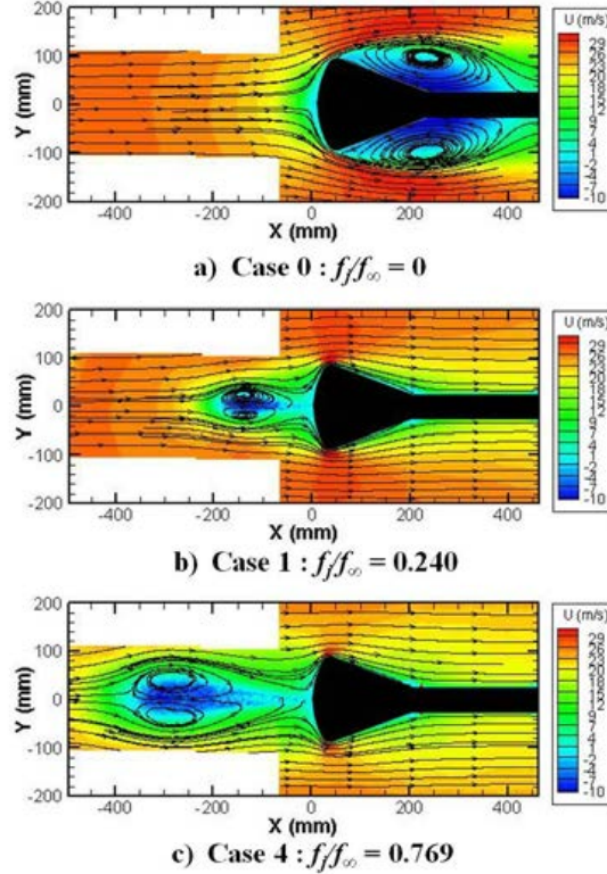


Figure 3.2: Velocity distribution using PIV measurement of a vehicle performing sub-sonic retro-propulsion. Courtesy of Nonaka et al. [13]

3.2 Real life vertical landing examples

In the recent years, the private sector has built and flown a couple of RLVs: the orbital Falcon 9 (SpaceX) and the sub-orbital New Shepard (Blue Origin) vehicles. Figures 3.3a and 3.3b show both vehicles during their landing burn maneuvers. Table 3.3 compares the flight conditions and the vehicle specifications of both spacecraft.

Table 3.3: Parameters for each vehicle at the start of their landing burn [7, 8, 33, 34] (*estimated values, **@70% thrust).

Parameter	Symbol	New Shepard	Falcon 9	Unit
Engine	-	BE-3	Merlin-1D	-
Propellant	-	LO2/LH2	LO2/RP-1	-
Freestream velocity	u_∞	160	350	m/s
Altitude	H	650	4000	m
Ambient pressure	p_a	0,94	0,70	bar
Thrust range	F	(90, 490)	(482, 845)	kN
Max. chamber pressure	p_0	87*	97	bar
Est. nozzle pressure ratio**	p_0/p_a	65*	97*	-
Freestream momentum flux	f_∞	230*	1096*	kN
Momentum flux ratio**	f_j/f_∞	1,5*	0,54*	-



(a) $f_j/f_\infty \approx 1,5$; NPR ≈ 65



(b) $f_j/f_\infty \approx 0,54$; NPR ≈ 97

Figure 3.3: The New Shepard [31] (a) and two Falcon 9 boosters [32] (b) performing their landing burn maneuvers.

Some observations about the emerging flowfields can be made. For example, the interaction between the jet and the freestream counter-flow can

Table 3.4: Vehicle geometrical parameters [33, 34] (*estimated values).

Parameter	Symbol	New Shepard	Falcon 9	Unit
Base diameter	D_{ref}	3,2*	3,7	m
Nozzle exit diameter	D_E	0,7*	0,92	m
Base to nozzle exit diameter ratio	D_E/D_{ref}	4,6*	4	-
Vehicle length	l_v	18	41*	m
Vehicle aspect ratio	$AR = l_v/D_{base}$	5,6*	11*	-

be appreciated in the above pictures. Some key takeaways are:

1. The jet roughly maintains its cross section area up to the stagnation point where it seizes against the counter flow and it forms into a 'ball of fire' (a recirculation area) upstream behind the stagnation point.
The New Shepard's stagnation point extends further due to its higher f_j/f_∞ value, compared to the rather 'compressed' jet from the Falcon 9 with a lower f_j/f_∞ .
2. The behaviour of these real vehicles resembles the experimental results from Nonaka in figure 3.2.

3.3 Supersonic Retro-Propulsion Simulations

Previous numerical analysis on super-sonic retropropulsion potentially contribute comparable methodology and data about sub-sonic retro-propulsion. Ghosh et al. [10] study the aerospike nozzle in the context of SRP as an Entry, Descent, and Landing (EDL) method for Mars missions. Cordell et al. [35] do so similarly for conventional bell nozzles. Despite the higher complexity of SRP (with flow phenomena like jet and bow shock interactions), some observations on the flowfield, performance, and the evaluation method may be valuable in a sub-sonic environment.

Key takeaways are:

1. A notable flow feature of the SRP is that there exists a point called the *triple point*, where the supersonic free-stream flow, subsonic shock flow and the subsonic recirculating flow meet [36].

2. The pressure distribution on the vehicle body varies with the aerodynamic thrust coefficient ' C_T ' (and its corresponding nozzle pressure ratio p_0/p_a) due to the change in size and shape of the jet plume [35]. See figure 3.4. The thrust coefficient is defined in eq. 3.4, where F_x is the total thrust, $q_\infty = \frac{1}{2}\rho_\infty u_\infty^2$ is the dynamic pressure, and A_{ref} is the base surface area.

$$C_T = \frac{F_x}{q_\infty \cdot A_{ref}} = 2 \cdot \frac{f_j}{f_\infty} + \frac{A_E(p_E - p_\infty)}{q_\infty \cdot A_{ref}} \quad (3.4)$$

3. The thrust coefficient ' C_T ', the pressure ratios ' $\text{NPR} = p_0/p_a$ ' (chamber pressure to ambient pressure) and ' p_E/p_a ' (jet pressure at nozzle exit to ambient pressure) are useful to characterize the role of the jet in the flowfield.
4. In a SRP context, nozzle flows are usually studied in a high under-expanded state, corresponding to the typical low ambient pressure environments. NPR values are very high.

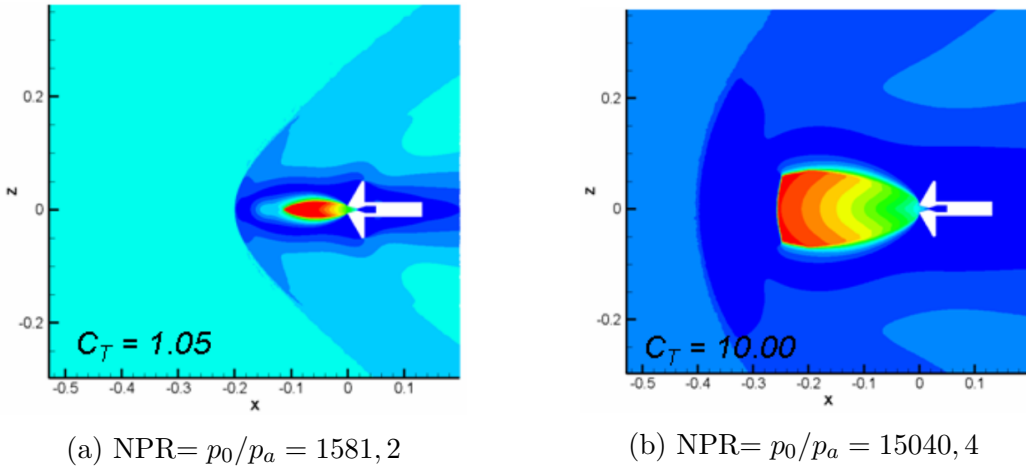


Figure 3.4: A SRP flowfield (RANS Mach contour) of a conventional nozzle with a low (a) and a high (b) thrust coefficient C_T . The freestream flows from left to right. Courtesy of Cordell et al. [35].

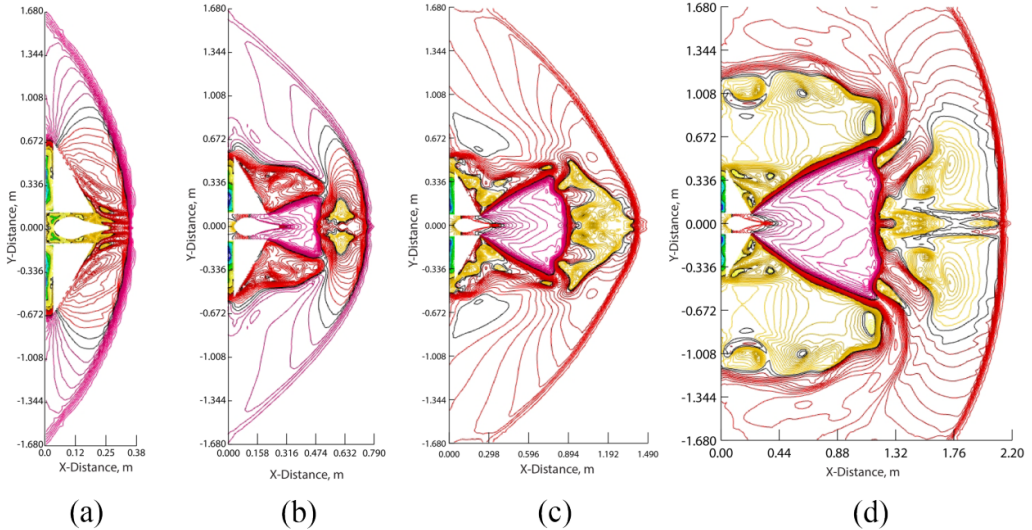


Figure 3.5: LES Mach number contours of an aerospike nozzle under SRP at different $\text{NPR} = p_0/p_a$ ratios: (a) 0, (b) 500, (c) 2200, (d) 8996. The freestream flows from right to left. Courtesy of Ghosh [10].

3.4 Cold flow tests of ANCs in subsonic retroflows

The planned cold-flow test campaign on ANCs in subsonic retro-flows by Scarlatella et al. [20] at the TUD provides an experimental tool to acquire data for the validation of an analogous simulation campaign. It also provides a methodology of analysis. This test campaign focuses on the performance of different ANCs (aerospike, DB nozzle, and ED nozzle) during a landing burn.

Test infrastructure

The test setup allows for the ad hoc investigation of the performance of different nozzle concepts under a conical subsonic counter-flow at different ambient pressures. A cold-gas nozzle test bench sits inside a vacuum wind tunnel (see figure 3.6 and 3.7).

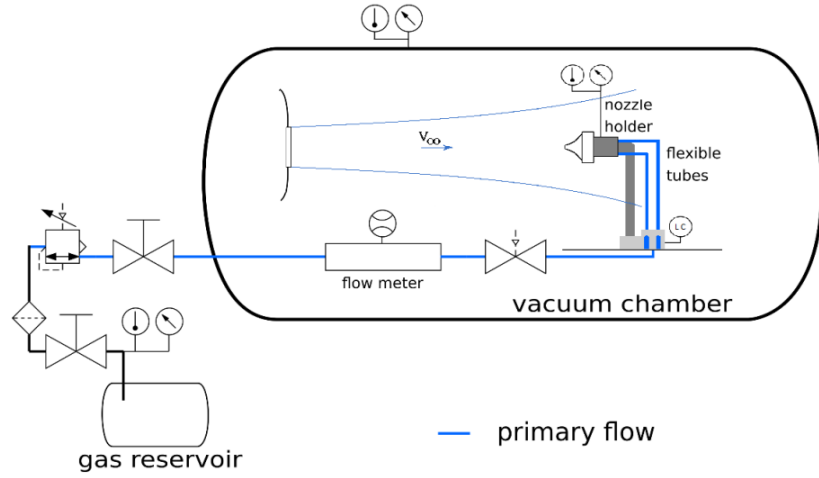


Figure 3.6: Schematic diagram of the test setup. Courtesy of Scarlatella [20].

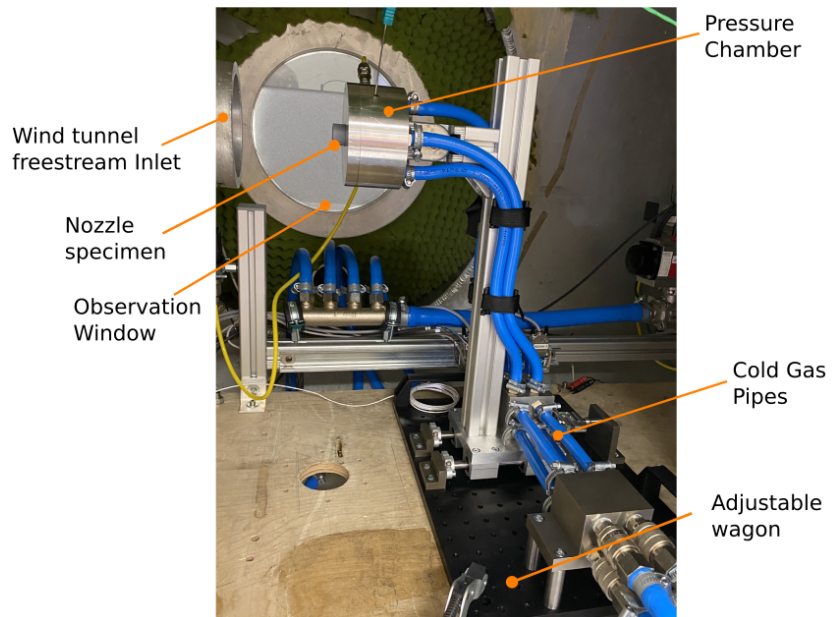


Figure 3.7: The test bench mounted inside of the wind tunnel. Modified picture courtesy of Roßberg [37].

The test bench is a slideable wagon that can adjust its distance to the

Table 3.5: Preliminary nozzle specimen design and pressure chamber parameters from Scarlatella et al. [20].

Parameter	Symbol	Jet off value	Unit
On design pressure ratio	$NPR_{o.d.} = p_0/p_a$	45	-
Chamber total pressure	p_0	4,8	bar
Chamber total temperature	T_0	293,15	K
Isentropic exponent	γ	1,4	-
Specific gas constant (air)	R	287	J/kgK
Nozzle expansion ratio	$\varepsilon = A_E/A_t$	4,82	-
Throat Area	A_t	58,8	mm^2
Mass-flow	\dot{m}_p	80	g/s
Thrust (o.d.)	$F_{o.d.}$	40	N

wind tunnel's freestream inlet plane. The wagon carries a structure that holds a pressure chamber (see figure 3.8) where a given 3D printed nozzle specimen is mounted on the base plate. This pressure chamber models the shape of the bottom of a rocket. Dry air is fed through the pipes, where it compresses and is forced to flow and expand through the given nozzle, generating thrust.

The wind tunnel can supply different ambient pressures and it provides a *conical* shaped countering freestream (see figure 3.9) at adjustable speeds. Additionally, preliminary design parameters for the nozzle specimens in investigation are defined as shown in table 3.5.

Sensors throughout the test bench measure the thrust ' F ', the chamber pressure ' p_0 ' and temperature ' T_0 ', the mass flow ' \dot{m}_p '. While sensors throughout the wind tunnel measure the ambient pressure ' p_a ', and the freestream velocity ' u_∞ '. For flow visualization, a Background-Oriented Schlieren (BOS) system is adopted through the observation window. Tables 3.6 and 3.7 summarize the technical specifications of the test setup.

Table 3.6: Vacuum wind tunnel specifications [38].

Parameter	Symbol	Value or range	Unit
Ambient pressure	p_a	0,1 - 1,01325	bar
Freestream jet velocity	u_∞	0 - 92	m/s
Freestream jet diameter (@inlet plane)	D_{u_∞}	100	mm
Tunnel diameter	D_{tun}	1200	mm
Tunnel length	l_{tun}	3400	mm
Observation window diameter	D_{win}	300	mm

Table 3.7: Pressure chamber geometrical specifications [37].

Parameter	Symbol	Value	Unit
Base plate diameter	D_{ref}	106	mm
Chamber assembly length	l_c	60	mm
Reference nozzle exit diameter	D_E	19	mm
Aspect Ratio	$AR = l_c/D_{ref}$	0,6	-
Base to nozzle exit diameter ratio	D_{ref}/D_E	5,6	-

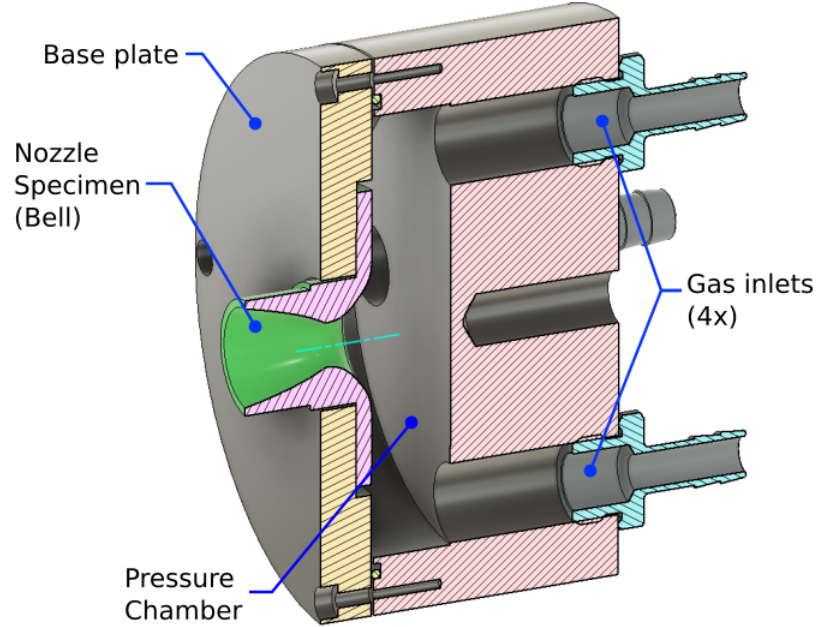


Figure 3.8: A half-section drawing of the pressure chamber assembly. Design courtesy of Roßberg [37]. The chamber configuration models the bottom of a rocket.

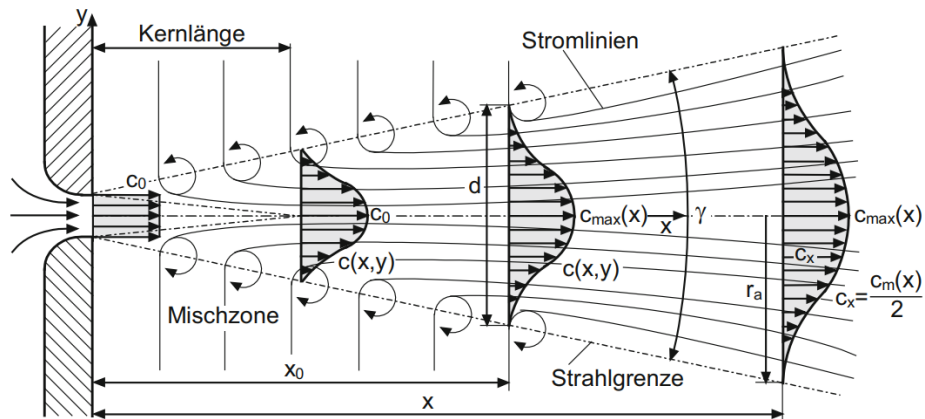


Figure 3.9: The flow profile of a conical flow jet [39]. The same profile is expected from the wind tunnel's freestream jet [40].

Methodology

Each ANC is tested and compared to a reference conventional bell nozzle under three distinct ambient conditions described in table 3.8. All nozzles are designed to share the same thrust level (ca. 40 N) at their design point of optimum expansion ($p_a = 0, 1067$ bar, at ca. 16 km of altitude according to table 3.5.).

Table 3.8: Test cases from Scarlatella et al. [20]. Each nozzle type is tested under these conditions.

Case	Time	Ambient pressure p_a	Counter-Flow	Main-Flow
1	steady	near-vacuum	no	yes
2	steady	sea level	no	yes
3	transient	near-vacuum to sea level	yes	yes

The testing includes cases without the counter-flow (1, 2) to allow for the validation of the nozzle designs and as a control case, to which the retro-propulsion case (3) will be compared.

The nozzle performance losses due to the interaction with the ambient pressure (divergence losses) are evaluated in terms of thrust ' F ' and the thrust coefficient ' C_F ', as defined in equations 3.4 and 3.6 [41].

$$F = C_F \cdot p_0 \cdot A_t \quad (3.5)$$

$$C_F = C_{F_{opt}} + \frac{A_E}{A_t} \cdot \left(\frac{p_E}{p_0} - \frac{p_a}{p_0} \right) \quad (3.6)$$

Where $C_{F_{opt}}$, defined in equation 3.7 is defined as the thrust coefficient corresponding to an optimal expansion ($p_a = p_E$) [41].

$$C_{F_{opt}} = \sqrt{\frac{2\gamma^2}{\gamma-1} \left(\frac{2}{\gamma+1} \right)^{\frac{\gamma+1}{\gamma-1}} \cdot \left[1 - \left(\frac{p_E}{p_0} \right)^{\frac{\gamma-1}{\gamma}} \right]} \quad (3.7)$$

The aerodynamic thrust coefficient C_T defined in equation 3.4 is used to characterize the aerodynamic performance of the retro-propulsion.

Key takeaways

Some key observations and takeaways are:

1. The cold gas test bench, and the chamber assembly provide a workable model to acquire experimental data about ANCs under sub-sonic retro-propulsion. This enables accessible flowfield visualisation and data for a CFD model validation.
2. The wind tunnel's applicability is limited since it provides a conical flow jet as freestream where $D_\infty \approx D_{ref}$. This does not correspond to the circumstances of a real landing maneuver, where the counter flow width is practically infinite ($D_\infty \gg D_{ref}$) and uniform (not conical).

This experiment arrangement may be applicable to extract values such as the of the aerodynamic thrust coefficient C_T and the momentum flux ratio f_j/f_∞ , but it does not provide realistic data on the drag and pressure coefficients (C_D and C_{p_i}) of a RLV, since the resulting flow around the body is incompatible.

3. The aspect ratio of the chamber assembly ($AR = 0, 6$) is not comparable to that of a usual RLV (e.g. the Falcon 9: $AR_{F9} = 11$). This likely produces an incomparable flowfield, especially downstream from the base.
4. The base to nozzle exit diameter ratio D_{ref}/D_E of the chamber assembly (5,6) is similar and comparable to that of real RLV (Falcon 9: 4 and New Shepard: 4,6).
5. Despite the limitations, this setup can provide an initial visualization of the flowfield topology. In particular, it can provide insights about the flow behaviour upstream from the base. For example:
 - at the stagnation point, where the main flow (jet) collides with the counter flow,
 - at the dissipative mixing layer between the jet's lateral boundaries and the freestream,
 - at the nozzle's exit plane and immediate vicinity. This should effectively display the altitude adaptive capabilities of the different ANCs.

- along the main flow exhaust plume/jet.
6. The method of analysis and the test bench can be easily moved, modified and extended to more complete and enhanced environments [20].
 7. Scarlatella's initial assessment is that the impact of the counter-flow on the altitude compensation efficiency should be minimal, but a drastic change in drag may be evident.

CHAPTER 4

Methodology

The objective of this thesis is to generate verified numerical simulation data about the flowfield and the performance of different ANCs under subsonic counter-flow. The data should be comparable to experimental campaigns for its validation, and it should be re-creatable. As a product, a verified and pre-validated CFD model for subsonic retro-propulsion should emerge. Then, an evaluation of the data comparing the performance of the different nozzles, particularly the aerospike nozzle, to a conventional nozzle is to be made.

Domain, geometry and boundary conditions:

To allow for validation, the simulation campaign is made analogous to the cold-flow test campaign by Scarlatella described in section 3.4. The numerical flowfield domains and geometries are defined based on this test infrastructure, and the same nozzle designs (for dry air) are used.

The flow boundary conditions for sub-sonic retro-propulsion are selected so that the momentum flux ratio f_j/f_∞ of the testing model (tested with $p_0 = 4,8$ bar at atmospheric pressure) matches with that of the landing burn of the SpaceX NROL-76 mission [8], and so that the f_j/f_∞ value lies within the experimental results of the Nonaka paper [13]. A target value of $f_j/f_\infty = 0,42$ is selected.

Furthermore, to take advantage of the versatility of CFD simulations, the

flow domain and boundary conditions will be adapted to correspond more closely to real flight conditions:

- the counter-flow freestream will be uniform and wide instead of conical and narrow. More concretely, the freestream to base diameter ratio will be $D_\infty/D_{ref} \geq 5$.
- the aspect ratio AR of the testing model will be extended to resemble a real RLV: $AR \approx 8$. For the simulation domain, only a portion of the booster model is included (2,5 times the cross section diameter in length), ignoring a portion of the skin friction drag and the wake pressure downstream from the vehicle. As a consequence, drag values are not realistic.
- The extent of the domain boundaries (inlet, farfield, and outlet) will be adapted to visualize and resolve relevant flow phenomena and it will not be constrained by the volume of the wind tunnel.

This setup should allow for a meaningful study of the jet/freestream interaction and the nozzle performance defined by the flow upstream from the base. At the same time it should allow for a meaningful study of the flow behaviour around the vehicle downstream from the base, enabling more accurate predictions of the pressure coefficients. The wake of the vehicle however is not modelled to contain the computational cost, this at the expense of some accuracy regarding the drag values.

Simulation model

A RANS type, steady state, 2D axis-symmetric simulation model will be developed using the academic license of the ANSYS Fluent software (max. 512k cells/nodes) and run with a home PC (double precision, 4 cores; 16 GB of RAM, Intel i7-3770K Processor, and an NVIDIA GeForce GTX 760 graphics card).

Simulation Campaign

Each nozzle will be set to the conditions shown in table 4.1 below:

Table 4.1: Simulation campaign conditions. The chamber pressure remains constant at $p_0 = 4,8$ bar. (*expected value)

Case	Description	p_a [bar]	$ u_\infty $ [m/s]	NPR [-]	f_j/f_∞ [-]
1	o.d. Static Burn	0,1067	0	45	-
2	SL Static Burn	1,01325	0	4,74	-
3	Aerodynamic Descent	1,01325	60	0	0
4	Sub-sonic Retro-propulsion	1,01325	60	4,74	0,42*

Where

- case 1 is used to validate the design of the nozzle in optimal expansion conditions,
- case 2 is the in situ reference case for the performance of the nozzle under sea-level conditions without the counter-flow,
- case 3 is the in situ reference case for the aerodynamic performance of the vehicle body under counter-flow without the jet/main-flow,
- and case 4 is the full in situ scenario of sub-sonic retro-propulsion.

Verification criteria

The simulations will be considered converged when the following criteria are met:

- All residual magnitudes lie below 10^{-5} .
- The following values converge monotonously for more than 100 iterations:
 - Momentum thrust ($f_j = \dot{m}_p \cdot v_p$)
 - Drag coefficient (C_D)

Evaluation

The flowfields for each case and nozzle will be visualized with contours of mach number and density gradient to show the shock wave patterns, and a contour of velocity with streamlines to observe the aerodynamic behaviour.

Then quantitative data about the aerodynamic and nozzle performance is extracted. All the used equations are defined or redefined here.

To evaluate *aerodynamic performance*, the pressure coefficient from a point on the booster's side face ' C_{p_s} ' (located at 1 diameter's length from the base) and a point on the booster's bottom face ' C_{p_b} ' (located at 2/3 of the radius from the axis) are obtained using equation 4.1.

$$C_{p_i} = \frac{p_i - p_\infty}{q_\infty} \quad (4.1)$$

Where

$$q_\infty = \frac{1}{2} \rho_\infty u_\infty^2 \quad (4.2)$$

Additionally, the momentum flux ratio ' f_j/f_∞ ', is also obtained, where ' A_{ref} ' is the cross section area of the booster's base.

$$f_j/f_\infty = \frac{f_j}{2q_\infty \cdot A_{ref}} = \frac{\dot{m}_p \cdot v_p}{\rho_\infty u_\infty^2 \cdot A_{ref}} \quad (4.3)$$

Next, to evaluate the *nozzle performance* based on Huzel and Huang [15], the thrust coefficient ' C_F ', axial thrust ' F_x ', and specific impulse ' I_{sp} ' are calculated using the following equations:

$$C_F = C_{F_{opt}} + \varepsilon \cdot \left(\frac{p_E}{p_0} - \frac{p_a}{p_0} \right) \quad (4.4)$$

where

$$C_{F_{opt}} = \sqrt{\frac{2\gamma^2}{\gamma-1} \left(\frac{2}{\gamma+1} \right)^{\frac{\gamma+1}{\gamma-1}} \cdot \left[1 - \left(\frac{p_E}{p_0} \right)^{\frac{\gamma-1}{\gamma}} \right]} \quad (4.5)$$

$$F_x = C_F \cdot p_0 \cdot A_t = \dot{m}_p \cdot v_p + A_E(p_E - p_a) \quad (4.6)$$

and

$$I_{sp} = \frac{F_x}{\dot{m}_p \cdot g_e} = \frac{F_x}{\dot{w}} \quad (4.7)$$

where

$$\dot{w} = A_t \cdot p_0 \cdot g_e \cdot \sqrt{\frac{\gamma \cdot \left(\frac{2}{\gamma+1} \right)^{\frac{\gamma+1}{\gamma-1}}}{R_{air} \cdot T_0}} \quad (4.8)$$

The results of each nozzle are then compared to each other and with the data from the literature review.

CHAPTER 5

Problem Definition and Pre-Analysis

For each nozzle configuration four distinct case scenarios are set. Each scenario has its own boundary conditions. Every case however shares these assumptions:

- Axis-symmetrical flow; the freestream and thrust vectors are co-linearly aligned to the booster's rotational axis of symmetry. Therefore the flow is assumed to behave symmetrically around this axis.
- Steady-state flow; the flow does not change with time, and all turbulence induced fluctuations are averaged using the RANS method.
- The freestream flow is assumed incompressible since its velocity remains sub-sonic and under $M = 0, 3$.
- The jet flow is assumed compressible since its speeds are far over $M = 0, 3$.
- All flows are assumed viscous and there is a no-slip condition on all walls.
- The working fluid is dry air as an ideal gas for both freestream and jet flows ($\gamma = 1, 4$ and $R_{air} = 287 \text{ J/kgK}$).

- At every boundary condition a standard sea level temperature T of 293,15 K (20°C) is assumed.

A description and pre-analysis is made for each case in more detail in the following sections.

5.1 Case 1: On-design Static Burn

In this first case, illustrated in figure 5.1, the nozzle design and its performance alone is investigated under optimal conditions.

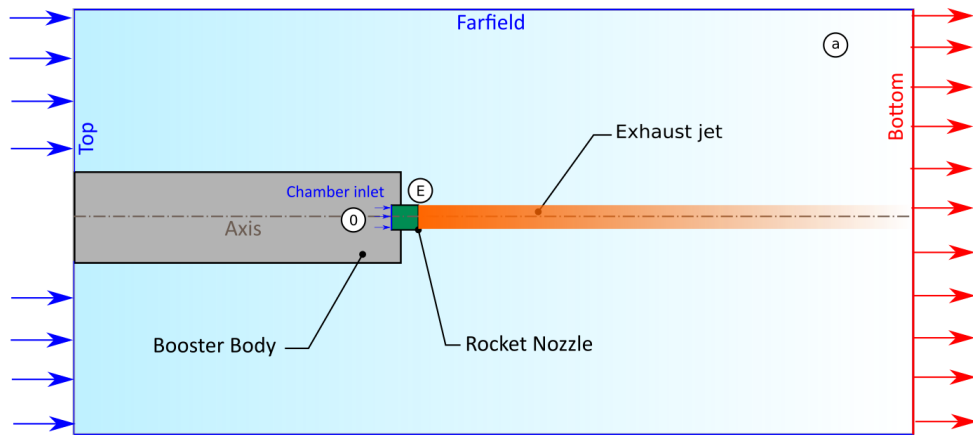


Figure 5.1: Case 1: On-design static burn problem schematic.

Table 5.1: Given parameters for Case 1. Optimal expansion static burn.

Parameter	Symbol	Value	Unit
Ambient pressure	p_a	0,1067	bar
Chamber pressure	p_0	4,8	bar
Expansion Ratio	ε	4,82	-
Ambient Temperature	T_a	293,15	K

Assuming isentropic flow and that $p_a = p_E$ (design conditions; $p_E/p_{E_{o.d.}} = 1$), the analytical results shown in table 5.2 were derived. Images 5.2a and 5.2b depict real hot fire tests of a bell and an aerospike on design conditions,

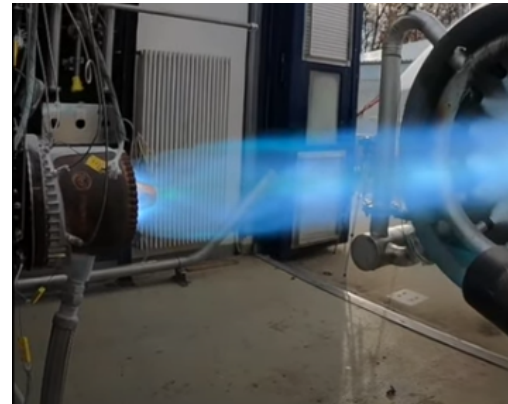
where their exhaust flow topology and shape can be observed. Images 5.3a and 5.3b show illustrations of the expected topology of the exhaust plumes.

Table 5.2: Analytical results for the performance of the conventional bell and aerospike nozzle in case 1.

Parameter	Symbol	Bell	Aerospike	Unit
Optimal Thrust Coefficient	$C_{F_{opt}}$	1,4751	1,4751	-
Thrust Coefficient	C_F	1,4751	1,4751	-
Axial Thrust	F_x	41,63	40	N
Propellant Weight Flow	\dot{w}	0,6532	0,6277	N/s
Specific Impulse	I_{sp}	63,72	63,72	s



(a) Airborne Engineering's Bell [42]



(b) Pangea's Aerospike [43]

Figure 5.2: The exhaust jets from a bell nozzle (a) and from an aerospike nozzle (b) on design conditions (optimal expansion).

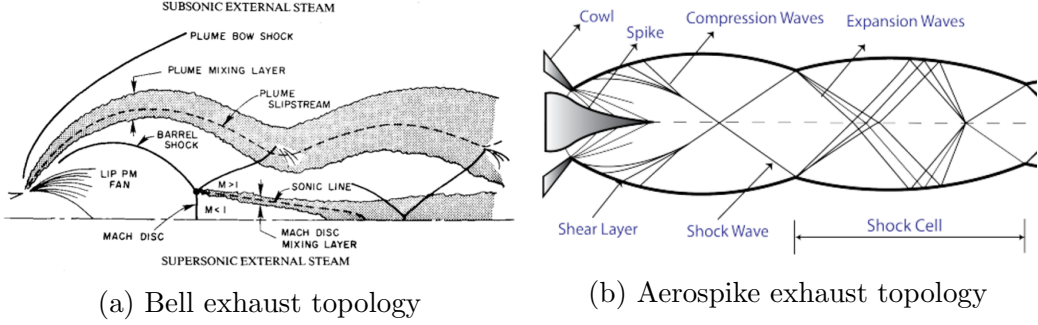


Figure 5.3: Illustrations and topology descriptions of the exhaust jets from a bell nozzle (a) and from an aerospike nozzle (b).

5.2 Case 2: Sea-level Static Burn

The setup for the second case is the same than case 1, except that the ambient pressure is at sea level conditions ($p_a = 1 \text{ atm}$). This causes the conventional nozzle to operate below its design point, leading to overexpansion. Since the operation to design exit pressure ratio is ($p_E/p_{a_{o.d.}} = 9,5 > 1$), the nozzle flow is expected to be highly over-expanded with early flow separation within the nozzle. Additionally, this condition predicts the presence of a normal shock wave within the nozzle, limiting the assumption of isentropic flow made in case 1, as flow through a normal shock is not isentropic.

To reduce the complexity of the pre-analysis calculations, the assumption of isentropic flow is sustained. This because it can offer a useful but coarse approximation about the nozzle performance. For a more accurate analytical prediction, the method explained by Anderson in reference [44] is recommended.

Table 5.3: Given parameters for Case 2. Sea-level static burn.

Parameter	Symbol	Value	Unit
Ambient pressure	p_a	1,01325	bar
Chamber pressure	p_0	4,8	bar
Expansion Ratio	ε	4,82	-
Ambient Temperature	T_a	293,15	K

Using the same equations from case 1, the nozzle performance is predicted

as shown in table 5.4.

Table 5.4: Analytical results for the performance of the conventional bell and aerospike nozzle in case 2.

Parameter	Symbol	Bell	Aerospike	Unit
Optimal Thrust Coefficient	$C_{F_{opt}}$	1,4751	1,0852	-
Thrust Coefficient	C_F	0,5647	1,0852	-
Axial Thrust	F_x	15,94	29,42	N
Propellant Weight Flow	\dot{w}	0,6534	0,6277	N/s
Specific Impulse	I_{sp}	24,4	46,9	s

In the case of the aerospike nozzle, the flow also works below its design point altitude, but in this case the flow is compressed onto the spike by the ambient pressure, where it 'slides' without separation and expands isentropically without any emerging normal shock waves. In contrast to case 1, the flow cross-section area is reduced to a narrower ring around the spike. For the aerospike, the equations for isentropic flow are used always assuming optimal expansion ($p_E/p_{a_{o.d.}} = 1$) below its design point, to correspond to its altitude adaptation capability. However, some efficiency losses are expected due to the spike's truncation for example.

5.3 Case 3: Aerodynamic Descent

For case 3, illustrated in figure 5.4, the booster has its engine off and is under free-fall with its axis parallel to the freestream flow vector. A wall of uniform and parallel flow at a sub-sonic speed ($u_\infty = 60m/s$) moves towards the bottom of the booster and on its nozzle. Because the flow is sub-sonic, the streamlines should adapt around the vehicle in a smooth continuous way. The flow should accelerate as it encounters the edges of the base plate and flow over and away from the booster's side wall. This creates flow separation from the base and a re-circulation zone along the wall, up to a certain extent where the flow reattaches on the top of the booster, if the vehicle is tall enough.

This kind of flow is very similar to the very well-studied flow around a pitot tube. The pitot tube, a device to measure dynamic and static pressure, is usually cylindrical in shape and it is placed parallel to the direction of

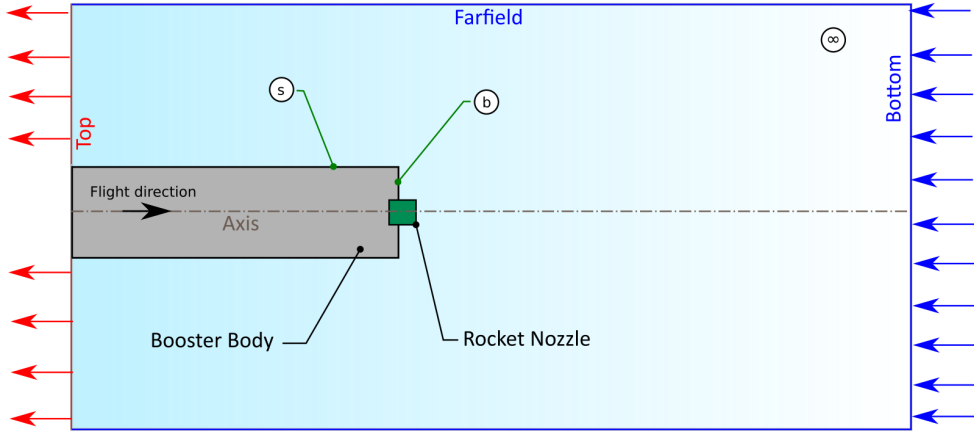


Figure 5.4: Case 3: Aerodynamic descent problem schematic.

flight. This condition arguably matches the one of a cylindrical booster in freefall. For this reason the flow around the booster is assumed to be equal to the flow around a Pitot Tube, documented in source [44].

For a pitot tube, its diameter is concretely defined while its length is defined non-dimensionally in terms of multiples of its diameter. An opening for a pressure sensor is placed on the frontal face and on the lateral face, where the lateral opening is placed at a certain distance from the frontal face. Reference [44] shows the predicted behavior (based on experimental data) of the pressure coefficients on the frontal opening, and on the lateral opening depending on its distance to the frontal face. For example, at the front a value of $C_{pb} = +1$ is predicted, while at a distance of 1 diameter along the side wall, a value of $C_{ps} = -0,85$ is expected. The C_{ps} then slowly converges to 0 as this distance increases and the flow reattaches. The same behavior around the booster is expected.

Additionally, because the freestream flow is sub-sonic it can be assumed incompressible. This allows the use of Bernoulli's equation. Any body forces coming from gravitational potential are neglected due to the small altitude differences (< 10 m). To predict the pressure on the base, Bernoulli's equation is applied to a streamline from the freestream. (The density is calculated for $T_\infty = 293,15K$ using the ideal gas law)

$$p_b + q_b = p_\infty + q_\infty \quad (5.1)$$

Rearranging to find the pressure at the base and inserting the given values

(assuming stagnation at the base $u_b = 0$):

$$p_b = p_\infty + q_\infty - q_b = p_\infty + q_\infty = 1,0349[\text{bar}] \quad (5.2)$$

Inserting this value on the pressure coefficient equation results in:

$$C_{pb} = \frac{p_b - p_\infty}{q_\infty} = 1 \quad (5.3)$$

And for the pressure at the side at 1 diameter distance from the base (using the experimental data that $C_{ps} = -0,85$):

$$p_s = C_{ps} \cdot q_\infty + p_\infty = 0,9948[\text{bar}] \quad (5.4)$$

Using Bernoulli's equation from the freestream to the side.

$$p_s + q_s = p_\infty + q_\infty \quad (5.5)$$

Rearranging for u_s with $q_s = \frac{1}{2} \cdot \rho_\infty \cdot u_s^2$:

$$u_s = \sqrt{(p_\infty + q_\infty - p_s) \cdot \frac{2}{\rho_\infty}} = 81,6[\text{m/s}] \quad (5.6)$$

This result predicts a max. freestream velocity increase of 40% due to the displacement by the vehicle.

Next a drag force and drag coefficient calculation would follow, but due to the fact that only a portion of the vehicle body is being considered (the pressure drag would be incomplete without the pressure on the top face from the wake) and that the calculation is too complex for the purposes of this thesis (especially for the calculation of the skin friction drag), the calculation is excluded. To show the detachment or attachment of the flow on the side wall, the side and base pressure coefficients (C_{ps} and C_{pb}) are monitored. These should imply the behaviour of the drag force and coefficient.

A summary of the expected results is shown in table 5.5:

Table 5.5: Predicted aerodynamic performance of the booster in case 3 for both nozzles.

Parameter	Symbol	Value	Unit
Freestream pressure	p_∞	1,01325	bar
Freestream velocity	u_∞	60	m/s
Pressure coefficient @side	C_{ps}	-0,85	-
Pressure coefficient @base	C_{pb}	1	-
Detached velocity @side	u_s	81,6	m/s

5.4 Case 4: Sub-sonic retro-propulsion

In the last case, illustrated in figure 5.5, the conditions from case 2 and 3 are combined, where the nozzle is activated under atmospheric conditions and its flow encounters a uniform parallel freestream flow. The total flow field is expected to change dramatically.

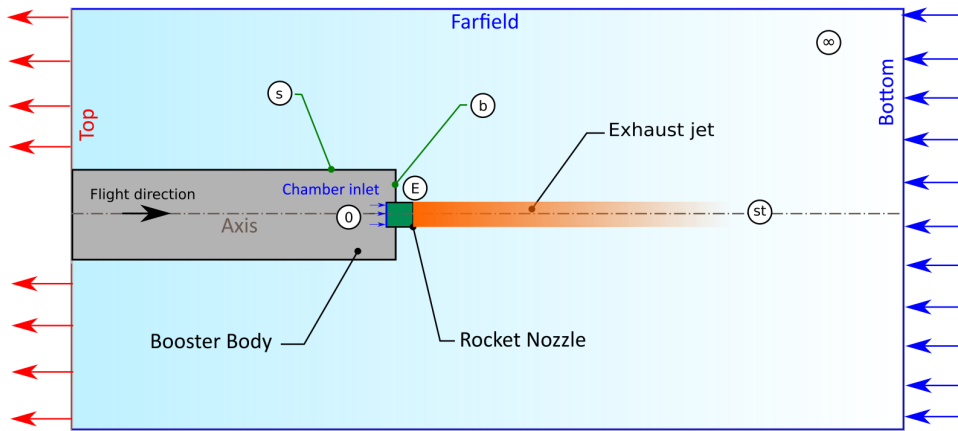


Figure 5.5: Case 1: Sub-sonic retro-propulsion problem schematic.

First, the aerodynamics aspect: based on the documented literature from Nonaka explained in section 5.3, a drastic change on the freestream flow surrounding the vehicle is expected. The central section of the freestream uniform wall encounters the exhaust jet through chaotic and turbulent momentum transfer. Its streamlines are expected to deflect in the radial di-

rection far upstream from the vehicle, and then ‘course correct’ and align themselves back to a parallel but denser configuration before approaching the vehicle body. This should lead to an attached flow on the vehicle side wall from the edge of the base along the entire length. This in contrast to case 3, where the flow is immediately detached.

Additionally, the flow-field directly upstream from the base is dominated by the nozzle exhaust flow. Its streamlines strongly emanate upstream from the nozzle exit along the jet up to the stagnation point (where $u_s = 0$), then bending outwards and back downstream towards the base plate edge, finally blending into the freestream along the body wall.

These flow field phenomena lead to a strong decrease of pressure on the base of the vehicle, and an increase of pressure on the sides of the vehicle. Therefore, the pressure drag decreases dramatically, while the skin friction drag increases moderately. This combination should lead to an overall dramatic decrease of the aerodynamic drag force and drag coefficient. The magnitude of the effect is correlated with the aerodynamic thrust coefficient (C_T) and/or momentum flux ratio (f_j/f_∞), as observed by Nonaka.

Secondly, regarding the nozzle performance and flow, a favorable change in the nozzle performance is expected in comparison to case 2. Due to the dynamic pressure increase near the base of the vehicle, a static pressure decrease at the nozzle exit is expected, allowing for a moderation of the over-expansion expected in case 2. This should result in an overall improved performance of the nozzle.

The static pressure and pressure coefficient at the side wall can be approximated using Bernoulli’s equation once again (the freestream flow is still incompressible and free of body forces).

Applying the equation from the freestream source to the side of the vehicle, and solving for the static pressure at the side p_s :

$$p_s = p_\infty + q_\infty - q_s \quad (5.7)$$

Assuming that $q_\infty \approx q_s$, then:

$$p_s = p_\infty \quad (5.8)$$

Next to predict the pressure at the base and the nozzle exit, assuming they are equal ($p_b = p_E$), we can assume that the jet flow, after reaching the stagnation point, is also incompressible and isentropic. This allows the use

of Bernoulli's equation once again, from the stagnation point 'st' to the base 'b'.

This assumption is rather weak, because the flow is highly turbulent and chaotic near the stagnation point and temperature gradients are high, possibly leading to high amounts of heat transfer. These are mechanisms for energy dissipation, that would break the isentropic assumption. However, the flow can be considered incompressible because the maximum speed it can gain is that of the freestream, which also lies in the sub-sonic regime.

Nevertheless, to reduce the complexity of the calculations, this assumption is pushed through. Using Bernoulli's equation from the stagnation point (where $u_{st} = 0$) towards the edge of the base, and solving for p_b (assuming that $p_s = p_\infty$, $q_s = 0$, and $q_b = q_\infty$) results in:

$$p_b = p_E = p_{st} + q_{st} - q_b = 0,992[\text{bar}] \quad (5.9)$$

From this the pressure coefficients at the base can be calculated:

$$C_{pb} = \frac{p_b - p_\infty}{q_\infty} = -1 \quad (5.10)$$

$$C_{ps} = \frac{p_s - p_\infty}{q_\infty} = 0 \quad (5.11)$$

The nozzle performance parameters are calculated in the same way than in case 1 and 2, the only difference is that the exit pressure does not equal the ambient pressure anymore, it is equal to the base pressure calculated in equation 5.9. Table 5.6 shows the expected nozzle performance values, while table 5.7 shows the expected aerodynamic performance values.

Table 5.6: Analytical results for the performance of the conventional bell and aerospike nozzle in case 4.

Parameter	Symbol	Bell	Aerospike	Unit
Optimal Thrust Coefficient	$C_{F_{opt}}$	1,4751	1,0911	-
Thrust Coefficient	C_F	0,5865	1,0911	-
Axial Thrust	F_x	16,55	29,59	N
Propellant Weight Flow	\dot{w}	0,6534	0,6277	N/s
Specific Impulse	I_{sp}	25,33	47,13	s
Aerodynamic thrust coefficient	C_T	0,87	1,55	-

Table 5.7: Predicted aerodynamic performance of the booster in case 3 for both nozzles.

Parameter	Symbol	Value	Unit
Freestream pressure	p_∞	1,01325	bar
Freestream velocity	u_∞	60	m/s
Pressure coefficient @side	C_{ps}	0	-
Pressure coefficient @base	C_{pb}	-1	-

CHAPTER 6

Nozzle Specimen Design

Using the parameters defined in table 3.5, a conventional bell nozzle and an aerospike nozzle are designed. Both designs share a $F_x = 40$ N thrust force at design point conditions ($p_a = 0$, 1067 bar). Both are designed to be 3D printed with SLA technology and they are mounted onto the base plate of the chamber assembly (figure 3.8) from the test campaign.

6.1 Conventional Bell Nozzle Design

The conventional bell nozzle was designed using the Rao parabolic approximation method as described by Huzel and Huang [15]. A Python code (that can be found in github [45]) was developed where a user can input the nozzle parameters (throat radius ' r_t ', expansion ratio ' ε ', divergent inflection angle ' θ_n ', convergent half angle, ' θ_{con} ', convergence ratio ' β ', combustion chamber length ' l_{ch} ', convergent radius ' r_{con} '). As a result, the code exports a comma separated value (.csv) file with the contour line of a bell nozzle in the form of a series of point (x,y,z) coordinates. This file can be then read with a CAD program (Fusion 360 for example) as a spline for further design.

For the nozzle design, the python function was called in the following way:

```
calculate_rao_nozzle(4.3263, 4.82, 50, 50, 3.467166, 8, 5)
```

The resulting contour and adapted design is shown in figures 6.1 and 6.2. Figure 3.8 shows the conventional bell nozzle integrated into the chamber assembly.

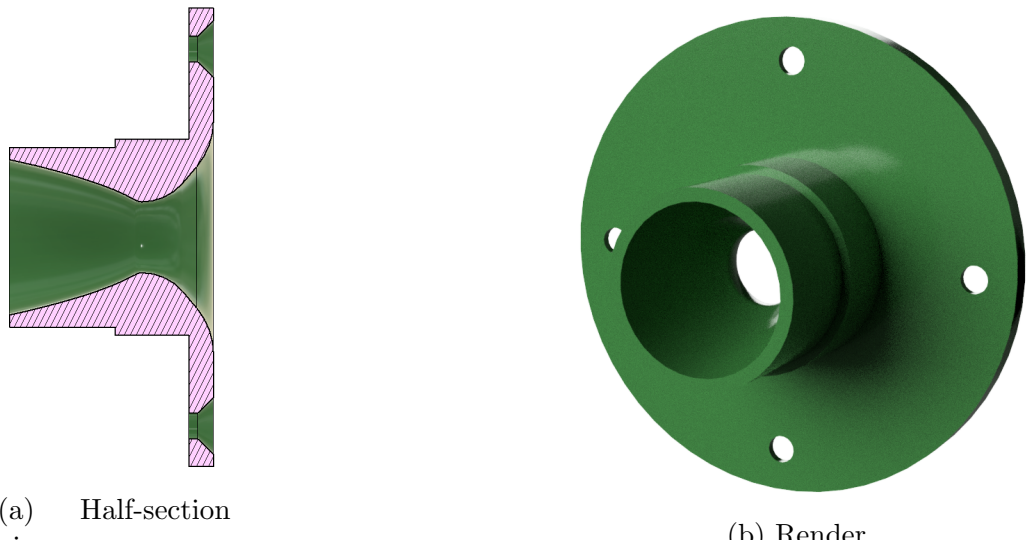


Figure 6.1: The conventional bell nozzle design for the test campaign. Design courtesy of Roßberg [37].

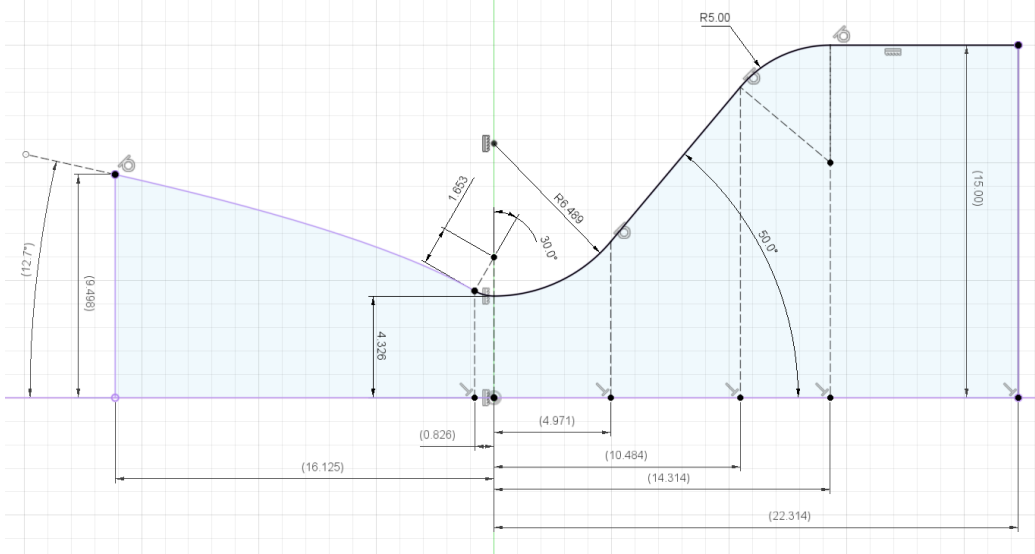


Figure 6.2: The contour drawing of the conventional Bell adapted for the simulation campaign. The converging part (right from the throat) is simplified. The units are in millimeters.

6.2 Aerospike Nozzle

The aerospike nozzle was designed using a python code developed by Matt Vernacchia [46] based on C.C. Lee's contouring method. A 45% truncation was selected to resemble the shape of the aerospike nozzle from the company Pangea Aerospace [43]. The program's GUI was filled in with data as shown in figure 6.3.

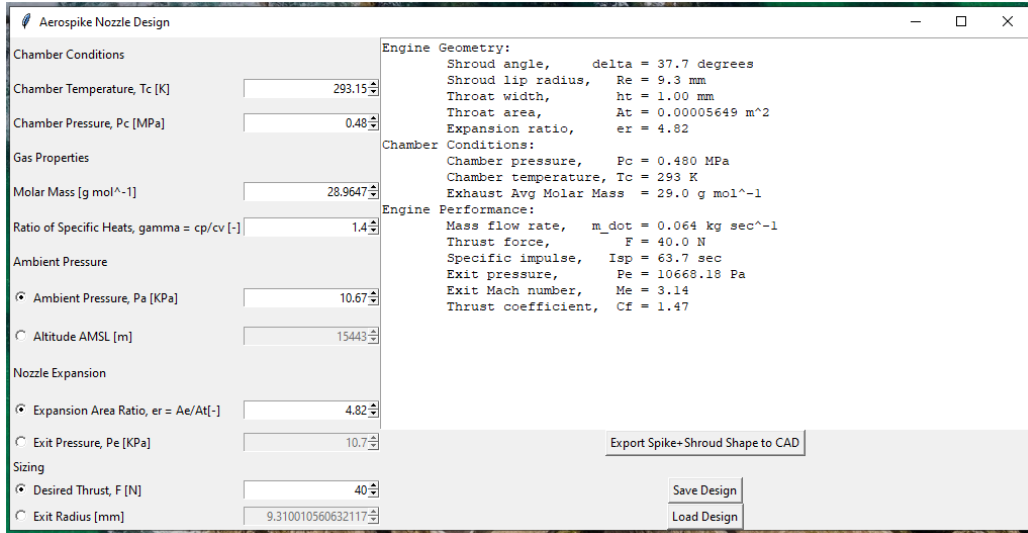


Figure 6.3: The settings used in the program's GUI to design the Aerospike contour with its corresponding expected performance.

The program exports two separate '.csv' files with the contours of the spike and the shroud in the form of a series of point coordinates. These were also imported to a CAD software (Fusion 360) and modelled further. The resulting design is shown in figures 6.4 and 6.5. Figure 6.6 shows it integrated into the chamber assembly. The spike and the shroud were connected using six NACA 0016 profiles as spokes to fix the spike in place.



(a) Frontal view (render).



(b) Back view (render).

Figure 6.4: The aerospike nozzle design for the test campaign.

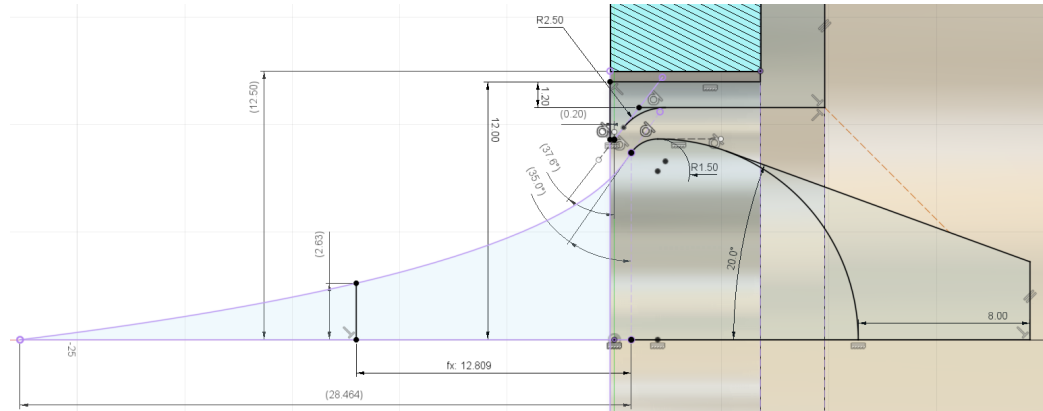


Figure 6.5: The contour drawing of the aerospike nozzle. The units are in millimeters.

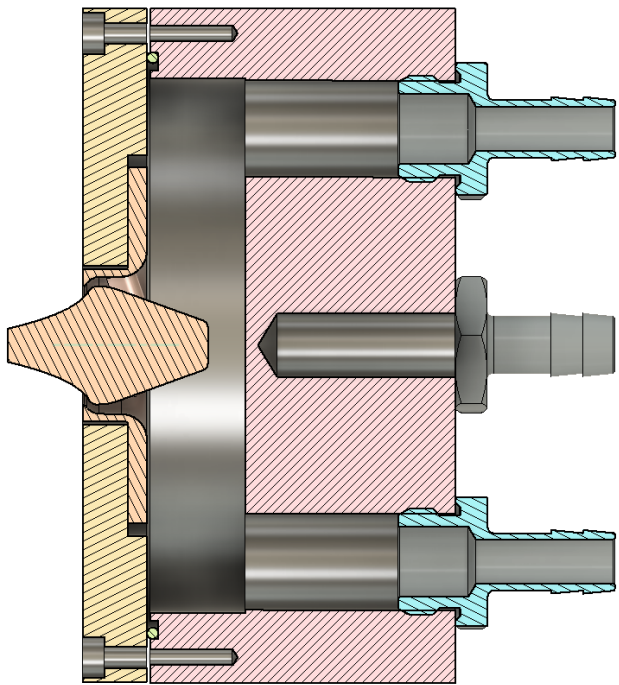


Figure 6.6: Half-section view of the aerospike nozzle design integrated into the chamber assembly.

CHAPTER 7

Domain Definition and Discretization

7.1 Domain definition

The flow domain should be selected to capture and resolve the characteristic qualities of the flow-field of a booster during a sub-sonic retro-propulsion maneuver. These qualities include:

- the nozzle flow acceleration and expansion into supersonic speeds,
- the shear/viscous boundary layer between the nozzle flow and the nozzle inner walls,
- its resulting exhaust jet with its forming shock and expansion waves (shock diamonds, mach disks, etc.),
- the turbulent mixing layer between the jet and the freestream flow
- the stagnation point and its immediate surroundings where the jet and the opposing freestream collide,
- the shear/viscous boundary layer around the booster's external walls (flow detachment or attachment),
- the wake downstream from the booster's top face,

- and the freestream streamline adaptation in the vicinity (beyond the boundary layer) of the booster.

At the same time, the domain should be optimized and simplified as much as possible to reduce the computational cost, without compromising the simulation quality. Since the scope of this investigation is constrained to the effects of a sub-sonic counter-flow on nozzle performance, and on the flow behaviour around the booster in a zero angle-of-attack configuration, the domain (shown in figure 7.1) was designed to capture all the qualities described in the list above, dismissing the flowfield qualities downstream from the booster.

To be exact, the domain excludes the flowfield beyond a distance of 2,5 times the cross-section diameter downstream from the base wall. This excludes the wake flow behind the booster and part of the boundary flow along the side wall, constraining the model's capability to predict the booster's drag force and drag coefficient accurately. This because the pressure and skin friction drag components would be incomplete. However, how and where the flow detaches or attaches is still observable, and its effect (at least qualitatively) on the drag can be inferred.

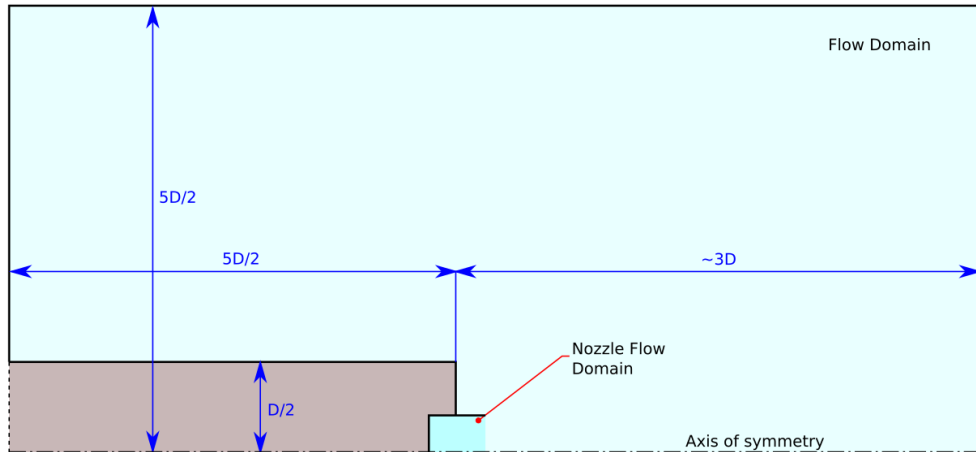


Figure 7.1: The flow domain (light blue) and its dimensions. $D = D_{ref} = 106$ mm is the diameter of the booster. The nozzle flow domain portion drawn here is generic and simplified.

Laterally, or in the radial direction from the booster's axis of symmetry, the domain only extends to 5 times the booster radius, enough to capture

the boundary layer and the freestream flow adaptation around the booster. Upstream, below the booster's bottom, the domain extends just enough to capture the stagnation point at a distance of ca. 2,8 times the booster's diameter from the base wall. Its position was found after an iterative process.

Finally, but most importantly, the domain is constrained to a quasi-two-dimensional axis-symmetric approach that only considers a small angle slice of a 'rotated cylinder'. With the assumption that the flow is symmetric about the booster's axis, which is a reasonable assumption in a steady flight with a zero angle-of-attack.

7.2 Discretization

Because the flow qualities of sub-sonic retro-propulsion at sea-level (case 4) result from a composition of the qualities from a sea-level 'static burn' (case 2) and a sea-level aerodynamic descent (case 3), the same domain and discretization/mesh are used for all 4 cases. Only differentiated by some details along the nozzle flow where the mesh is adapted to resolve the very thin shock waves (ca. 25 nanometers thick [47]), characterized by high pressure and density gradients.

A structured mesh configuration was selected, where the domain is subdivided in smaller domains to adapt to the geometry and to achieve high resolution in the areas with complex flow.

7.2.1 Mesh: Conventional bell configuration

Boundary layer at the nozzle wall

To resolve the boundary layer at the nozzle wall, an inflation layer was built by roughly calculating the maximum distance from the nozzle wall to the first cell center ' d^+ ' and the inflation layer count ' n_{lay} '. To calculate these values, the maximum possible velocity at the nozzle exit and its corresponding density value (assuming constant viscosity) were calculated from more simple simulations. The inflation layer count was guessed. Table 7.2 shows the values used for the calculation. An online calculator from source [48] was used. The resulting maximum distance is $d^+ = 0,02$ mm.

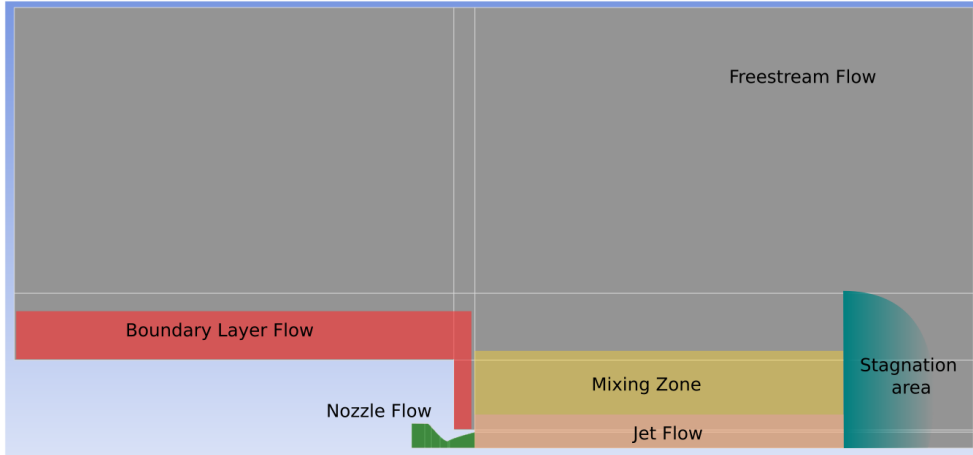


Figure 7.2: Mesh subdivision.

Table 7.1: Input parameters for the mesh inflation layer design at the nozzle wall.

Parameter	Symbol	Value	Unit
Velocity	u_{max}	660	m/s
Target $y+$	y_+	3	-
Density	ρ	0,224	kg/m^3
Viscosity	μ	$1,81 \cdot 10^{-5}$	Pa s
Layer count	n_{lay}	20	-

Boundary layer at the booster walls

The same process was made for resolving the boundary layer at the booster walls. In this case, the conditions from the freestream are used. Table ?? shows the values used for the calculation. The resulting maximum distance is $d^+ = 0,034$ mm.

Table 7.2: Input parameters for the inflation layer design at the booster walls.

Parameter	Symbol	Value	Unit
Velocity	u_{max}	60	m/s
Target $y+$	y_+	3	-
Density	ρ	1,224	kg/m^3
Viscosity	μ	$1,81 \cdot 10^{-5}$	Pa s
Layer count	n_{lay}	20	-

Table 7.3 describe the main properties of the mesh design, while figures 7.3 through 7.5 show the mesh design. Darker areas correspond to areas of high refinement/higher cell concentration. The aspect ratio of some cells is high only in areas where the flow is very simple and uniform (at the freestream).

Table 7.3: The main properties of the mesh (bell nozzle).

Parameter	Value	Comment
Cell count	222k	-
General growth rate	1,03	-
d^+ @ inner nozzle wall [mm]	0,013	$d^+ < 0,02$; $y^+ = 3$; OK
d^+ @ booster wall [mm]	0,03	$d^+ < 0,034$; $y^+ = 3$; OK
Avg. orthogonal quality	0,95	Excellent
Avg. skewness	0,1	Excellent
Avg. aspect ratio	4,8	Only poor in non-important areas

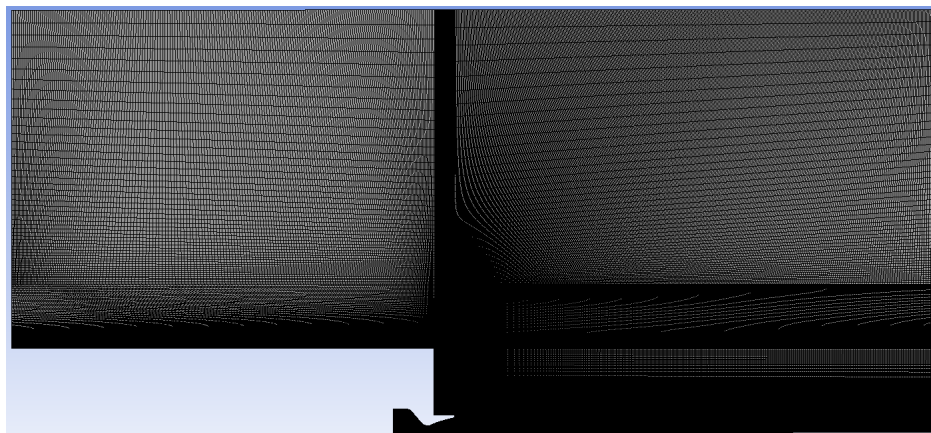


Figure 7.3: The mesh of the whole domain for the conventional bell nozzle configuration.

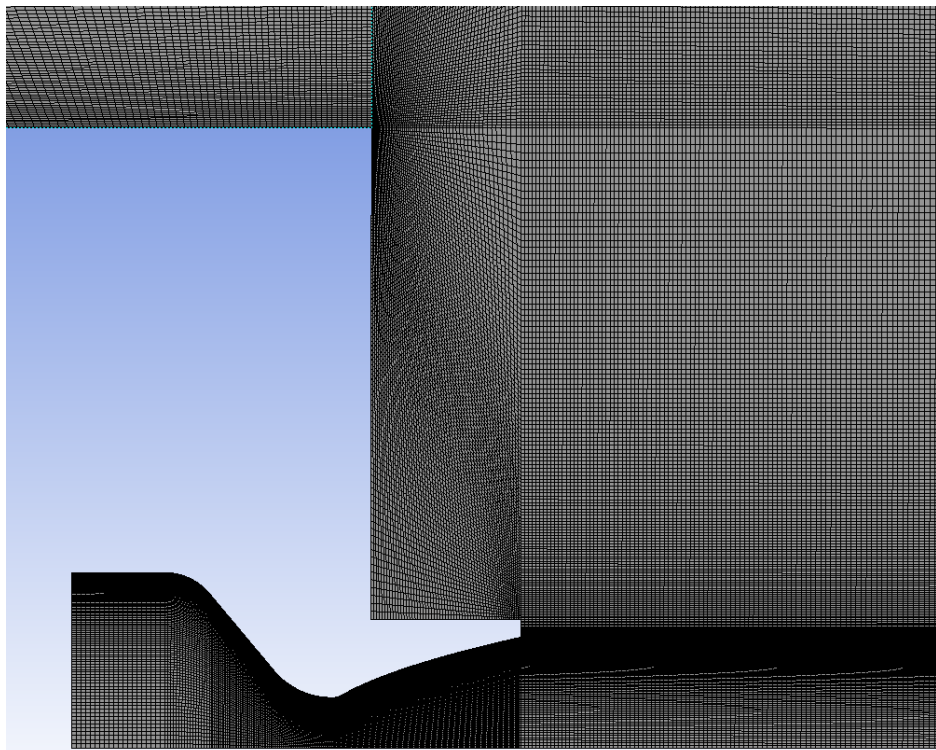


Figure 7.4: A close-up view of the mesh near the bottom face of the booster for the conventional bell nozzle configuration.

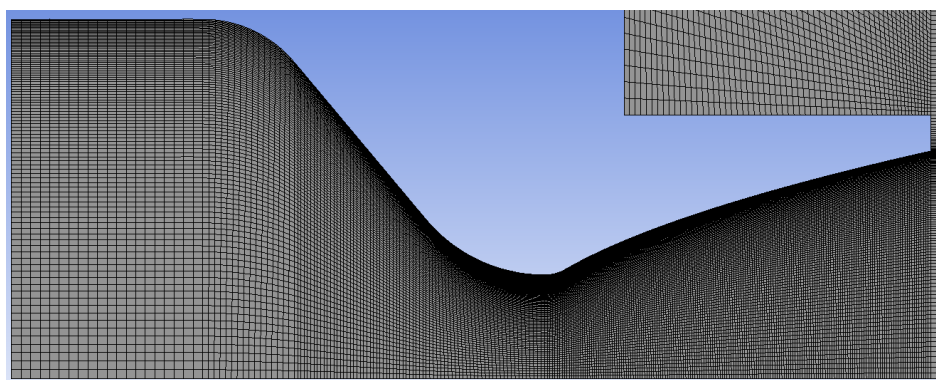


Figure 7.5: A close-up view of the mesh inside the conventional bell nozzle.

7.2.2 Mesh: Aerospike nozzle configuration

The mesh for the aerospike configuration was made in the same way than the conventional nozzle. The main differences are that the mesh inside the nozzle now has two inflation layers to capture the boundary flow over the shroud and spike walls. The same parameters (described in table 7.3) for the inflation layer inside the conventional bell were used for the one over the shroud and the spike. The rest of the mesh design is the same. Table 7.4 describes the main properties of the mesh. Figures 5.3 through 5.3 show the mesh design.

Table 7.4: The main properties of the mesh (bell nozzle).

Parameter	Value	Comment
Cell count	382k	-
General growth rate	1,05	-
d^+ @ spike and shroud walls [mm]	0,002	$d^+ < 0,02$; $y^+ = 1$; OK
d^+ @ booster wall [mm]	0,03	$d^+ < 0,034$; $y^+ = 3$; OK
Avg. orthogonal quality	0,94	Excellent
Avg. skewness	0,12	Excellent
Avg. aspect ratio	7,75	Only poor in non-important areas

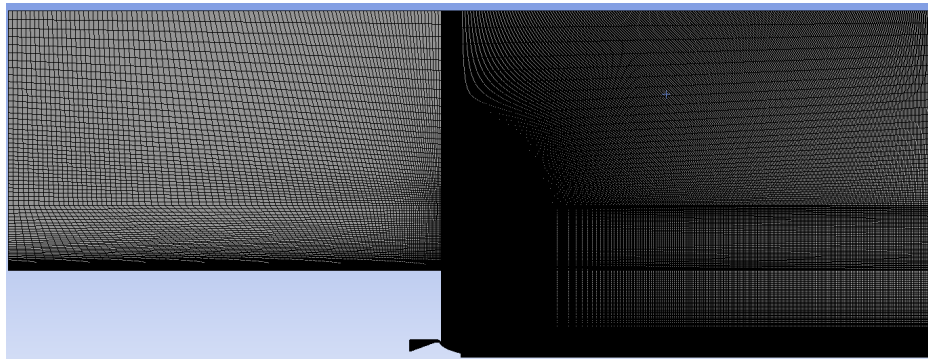


Figure 7.6: The mesh of the whole domain for the aerospike nozzle configuration.

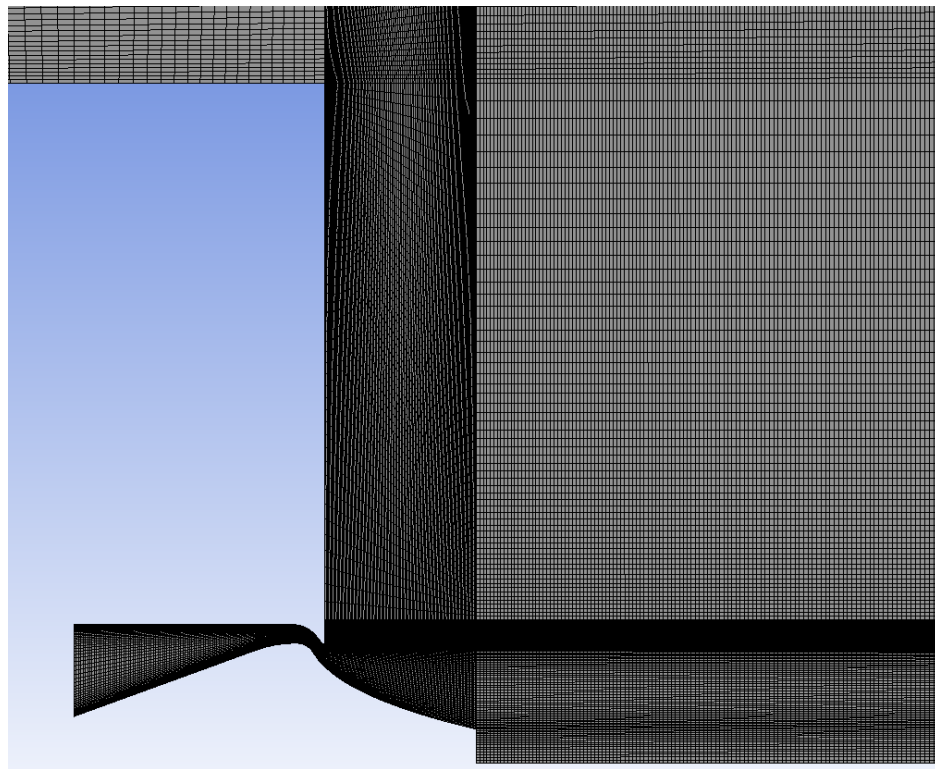


Figure 7.7: A close-up view of the mesh near the bottom face of the booster for the aerospike nozzle configuration.

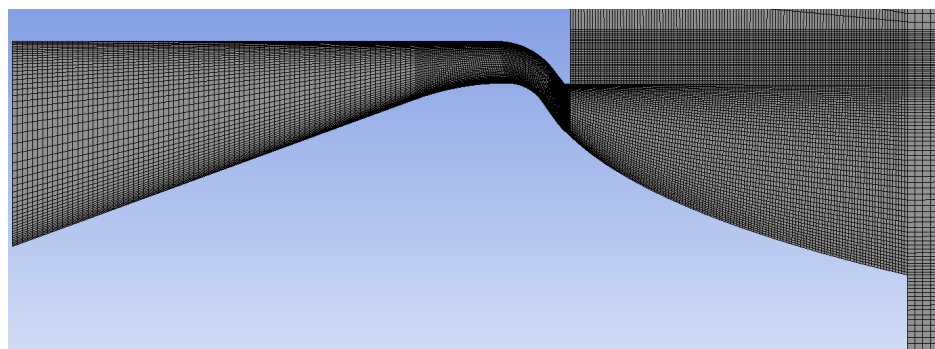


Figure 7.8: A close-up view of the mesh inside the aerospike nozzle.

CHAPTER 8

Simulation Model & Solution Setup

For both nozzles the same boundary conditions are set for each case. In general, the booster and nozzle walls are all set as 'wall' type, and all initial condition temperatures are set to 293,15 K. Figure 8.1 shows the nomenclature of each boundary. The nozzle inlet boundary condition's turbulence setting has a strong influence in the solution, therefore it was kept low (below 2%) and applied using the 'hydraulic diameter', defined by the geometric diameter at the pressure chamber (30 mm for the conventional bell, and 7 mm for the aerospike).

The energy equations are activated and the working fluid is always set to dry air, as an ideal-gas with Sutherland type viscosity. As a turbulence model, the k- ω -SST model is selected. Operating pressure is set to zero, and gravity is kept deactivated.

Every solution is first initialized using the hybrid method, followed by the full-multi-grid (FMG) initialization method. A pressure-based, steady and axisymmetric solver type is used. Solver methods are set to second order, with higher order term relaxation ticked (at 0,25 over all variables), and the solution controls are set to the software's default. Every residual (continuity, x-velocity, y-velocity, energy, k , and ω) is monitored to sink below 1e-5. The drag coefficient over the booster walls, and the thrust as a momentum flux over the nozzle exit area are monitored through the iterations to assess convergence.

Finally, after the first simulation converges, the mesh is refined for each case to resolve any emerging shock waves more clearly. This is done using the refinement function under domain adaptation, where the driving field variable is the density gradient.

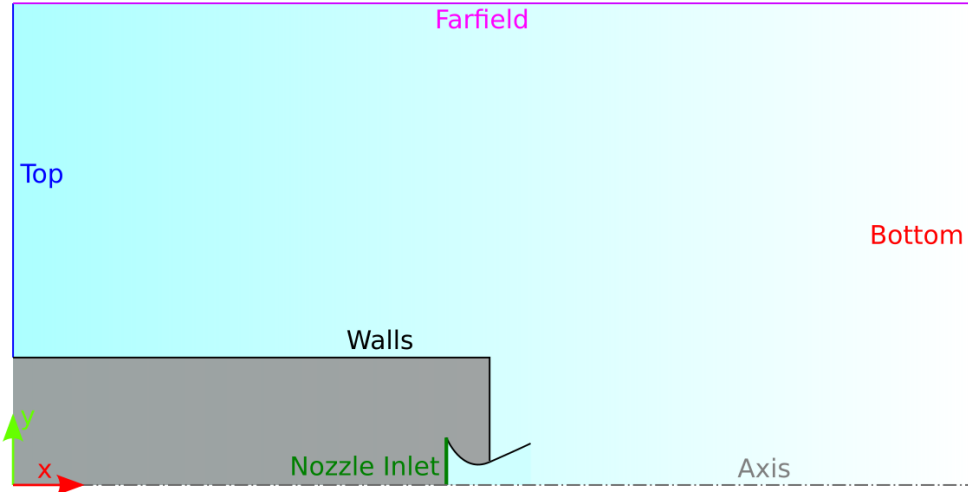


Figure 8.1: The simulation domain and its boundaries.

8.1 Case 1 Setup

For case 1, the nozzle is activated under design conditions without any counter-flow. The nozzle flow should create a suction effect, creating a light wind coming from the top boundary in the positive 'x' direction. To model this and ensure convergence stability in the simulation, the farfield boundary is set to have a 10 m/s flow in the positive direction. The ambient pressure overall is set to 0,1067 bar. The summary of the main boundary settings is shown in table 8.1.

Table 8.1: The main settings of the boundary conditions in case 1.

Boundary	Type	Characteristic Values
Nozzle Inlet	Pressure Inlet	4,8 bar; 2% turbulence
Top	Pressure Inlet	0,1067 bar
Bottom	Pressure Outlet	0,1067 bar
Farfield	Velocity Inlet	+10 m/s

8.2 Case 2 Setup

For case 2, the nozzle is activated under sea-level conditions without any counter-flow. The nozzle flow should also create a suction effect, creating a stronger wind coming from the top boundary in the positive 'x' direction. To model this and ensure convergence stability in the simulation, the farfield boundary is set to have a 10 m/s flow in the positive direction as well. The ambient pressure overall is set to 1 atm. The summary of the main boundary settings is shown in table 8.2.

Table 8.2: The main settings of the boundary conditions in case 2.

Boundary	Type	Characteristic Values
Nozzle Inlet	Pressure Inlet	4,8 bar; 2% turbulence
Top	Pressure Inlet	1,01325 bar
Bottom	Pressure Outlet	1,01325 bar
Farfield	Velocity Inlet	+10 m/s

8.3 Case 3 Setup

For case 3, the nozzle is not activated and the booster is under sea-level conditions with a 60 m/s counter-flow, where the freestream flows from the bottom boundary towards the top with a vector pointing in the negative 'x' direction. The ambient pressure overall is set to 1 atm. The summary of the main boundary settings is shown in table 8.3.

Table 8.3: The main settings of the boundary conditions in case 3.

Boundary	Type	Characteristic Values
Nozzle Inlet	Wall	-
Top	Pressure Outlet	1,01325 bar
Bottom	Velocity Inlet	-60 m/s
Farfield	Velocity Inlet	-60 m/s

8.4 Case 4 Setup

Finally for case 4, the nozzle is activated under sea-level conditions with a 60 m/s counter-flow, where the freestream flows from the bottom boundary towards the top with a vector pointing in the negative 'x' direction. The ambient pressure overall is set to 1 atm. The summary of the main boundary settings is shown in table 8.4.

Table 8.4: The main settings of the boundary conditions in case 4.

Boundary	Type	Characteristic Values
Nozzle Inlet	Pressure Inlet	4,8 bar; 2% turbulence
Top	Pressure Outlet	1,01325 bar
Bottom	Velocity Inlet	-60 m/s
Farfield	Velocity Inlet	-60 m/s

CHAPTER 9

Results and Post-Processing

Depending on the case, a color contour of mach number and of density gradient are produced to observe the qualities of the nozzle flow, and a color contour of velocity, and of turbulent kinetic energy are produced to observe the qualities of the free-fall flowfield and the sub-sonic retro-propulsion flowfield.

The performance of the nozzles is assessed quantitatively in the following way:

1. The axial thrust ' F_x ' is measured by adding the momentum and pressure thrust (the first and second terms of equation 2.1). The momentum thrust is calculated by measuring the velocity flow rate over the nozzle exit area, and the pressure thrust by multiplying this area with the simulated pressure difference between the nozzle exit and the ambient. The aerospike nozzle must add the truncation thrust as well, where the pressure at this wall is multiplied by its area.

In the case of the conventional bell nozzle, the nozzle exit area is found straight forward at the end of the nozzle. While in the case of the aerospike, the nozzle exit area is defined here as a 'donut' shaped area at the tip of the spike, where the inner radius is defined by the radius of the spike at the truncated tip, and the outer radius by the shroud radius at the throat.

2. The specific impulse is then calculated using equation 4.7 with the mass flow measured over the throat area and a the standard gravitational pull of earth $g_e = 9,81 \text{ m/s}^2$.
3. The thrust coefficient is calculated using equation 3.6, solving for ' C_F ' and inserting the simulated values for ' p_0 ' and ' F_x '.
4. For reference, the nozzle pressure ratio $NPR = p_0/p_a$ and the pressure expansion ratio p_E/p_a are calculated, where p_E is the average static pressure over the nozzle exit area.

The aerodynamic performance is assessed quantitatively in the following way:

1. The base and side pressure coefficients ' C_{pb} ' and ' C_{ps} ' are calculated by measuring the vertex average pressure at these points and using equation 4.1.
2. The (incomplete) drag force ' D ' and drag coefficient ' C_D ' is measured over the booster side and base walls, excluding the nozzle walls.
3. The momentum flux ratio ' f_j/f_∞ ' is calculated using the axial thrust ' F_x ' mentioned in the list above.
4. A plot of the velocity magnitude along the axis is used to observe the velocity fluctuations along the exhaust jet and to acquire the stagnation point location (where the velocity is zero) and its distance to the base ' l_{st} ' if applicable.

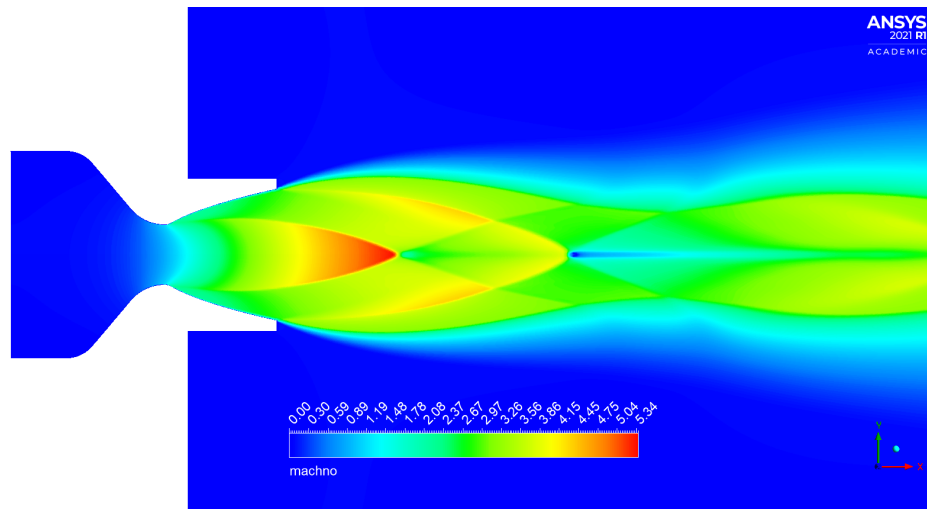
9.1 Case 1: On-design Static Burn

For case 1 only the qualities of the nozzle flow are to be analyzed. Attention is to be set on the nozzle flow optimal expansion, jet geometry, and shock waves. Table 9.2 show the simulated nozzle performance values for both nozzles.

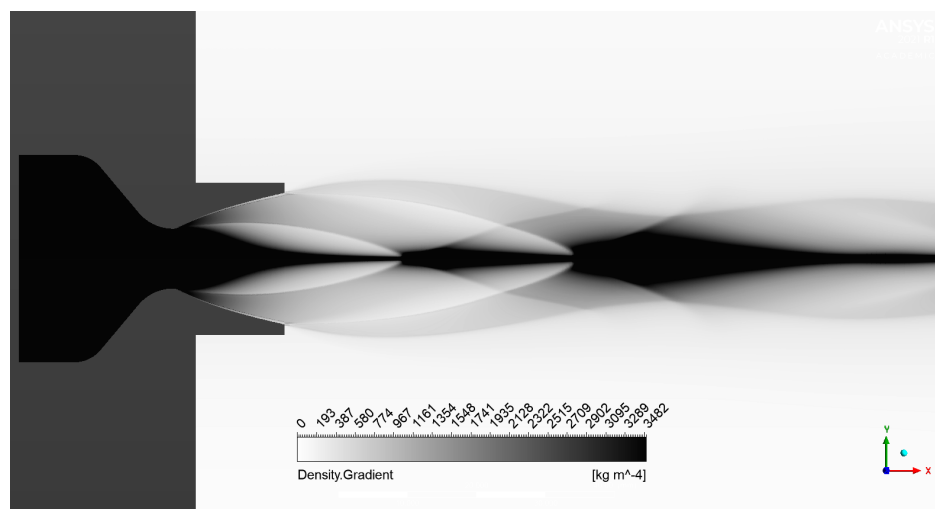
Table 9.1: Simulated nozzle performance values for the conventional bell and the aerospike nozzles in case 1.

Parameter	Symbol	Sim. Value		Unit
		Conv. bell	Aerospike	
Nozzle pressure ratio	p_0/p_a	45	44,7	-
Pressure expansion ratio	p_E/p_a	1,094	1,056	-
Axial thrust	F_x	-39,93	-36,89	N
Thrust coefficient	C_F	1,417	1,371	-
Specific impulse	I_{sp}	62,17	59,61	s

9.1.1 Conventional Bell Nozzle



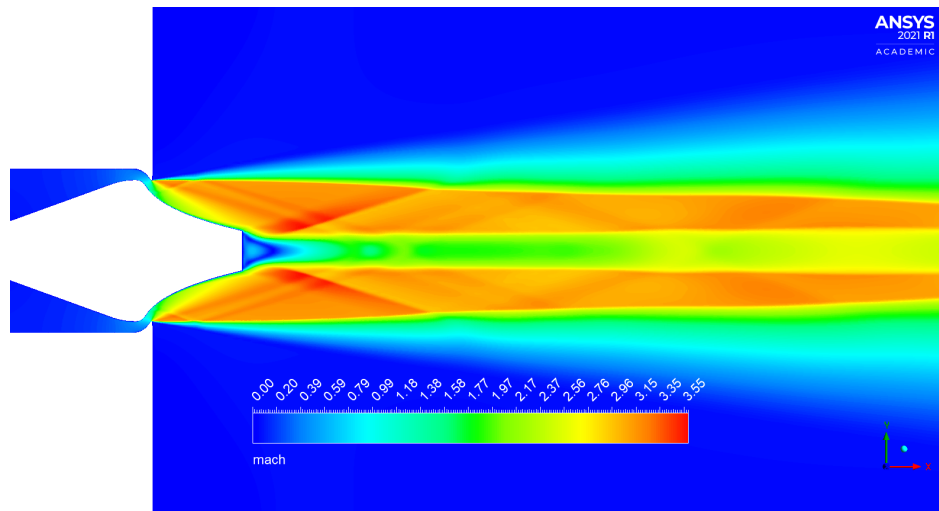
(a) Mach number Contour.



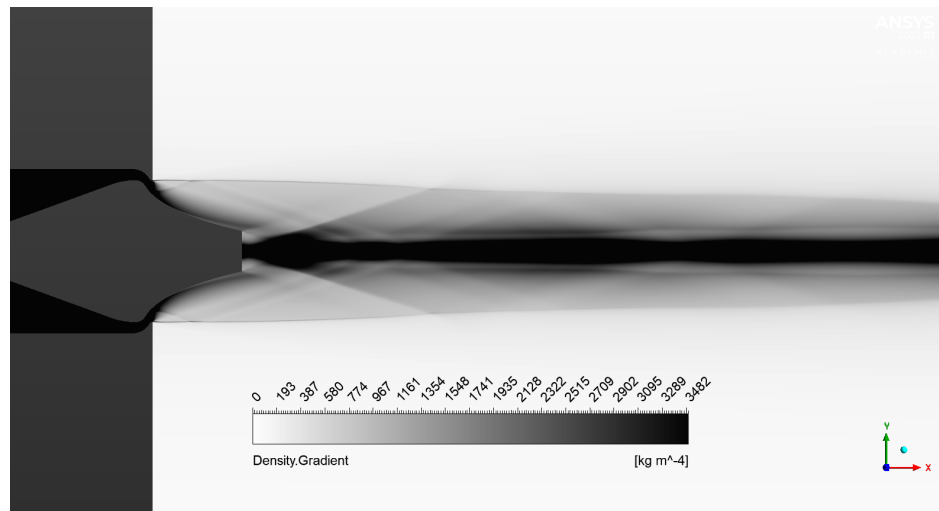
(b) Density gradient contour.

Figure 9.1: Contours of the flow in the aerospike nozzle under design conditions ($p_a = 0, 1067$ bar) (close-up view).

9.1.2 Aerospike nozzle



(a) Mach number Contour.



(b) Density gradient contour.

Figure 9.2: Contours of the flow in the aerospike nozzle under design conditions ($p_a = 0, 1067$ bar) (close-up view).

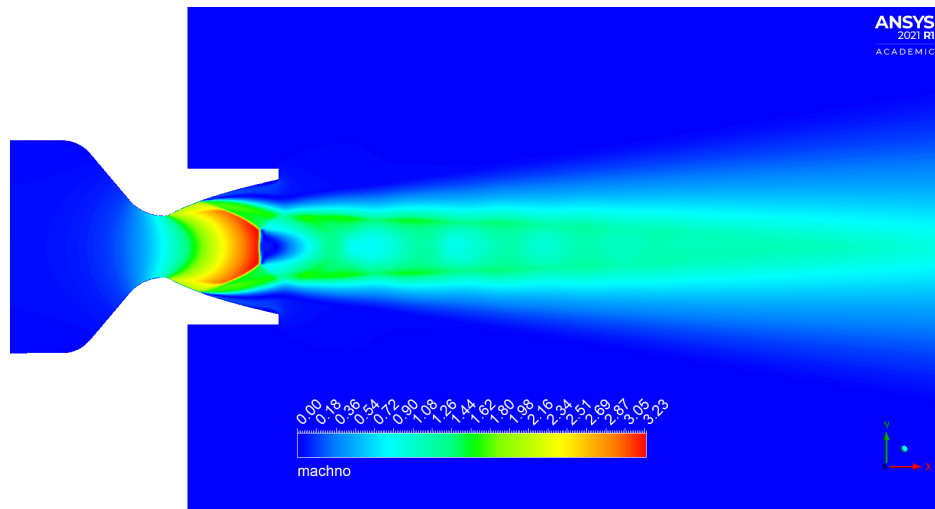
9.2 Case 2: Sea-level Static Burn

For case 2, similarly, only the qualities of the over-expanded nozzle flow are to be analyzed (1 atm = 1,01325 bar).

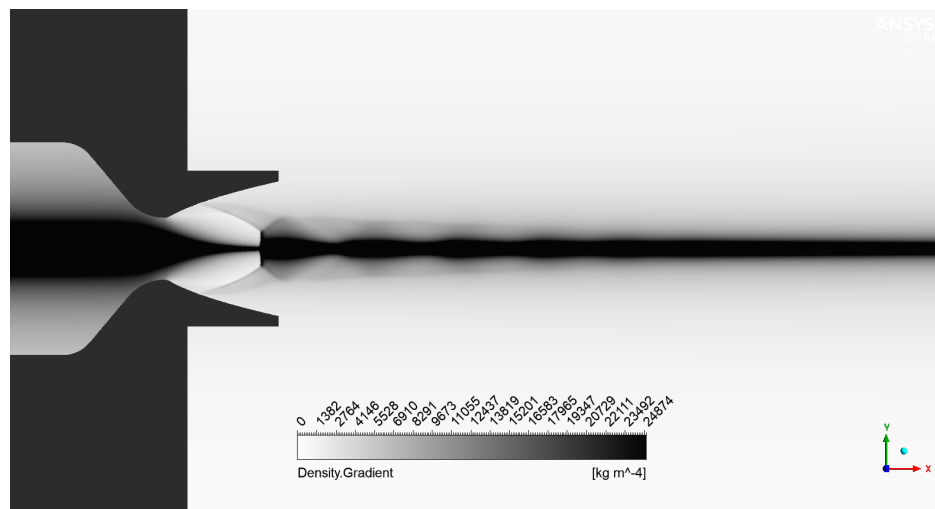
Table 9.2: Simulated nozzle performance values for the conventional bell and the aerospike nozzles in case 2.

Parameter	Symbol	Sim. Value		Unit
		Conv. bell	Aerospike	
Nozzle pressure ratio	p_0/p_a	4,73	4,704	-
Pressure expansion ratio	p_E/p_a	1,098	1,065	-
Axial thrust	F_x	-23,83	-30,43	N
Thrust coefficient	C_F	0,8454	1,129	-
Specific impulse	I_{sp}	36,78	49,1	s

9.2.1 Conventional Bell Nozzle



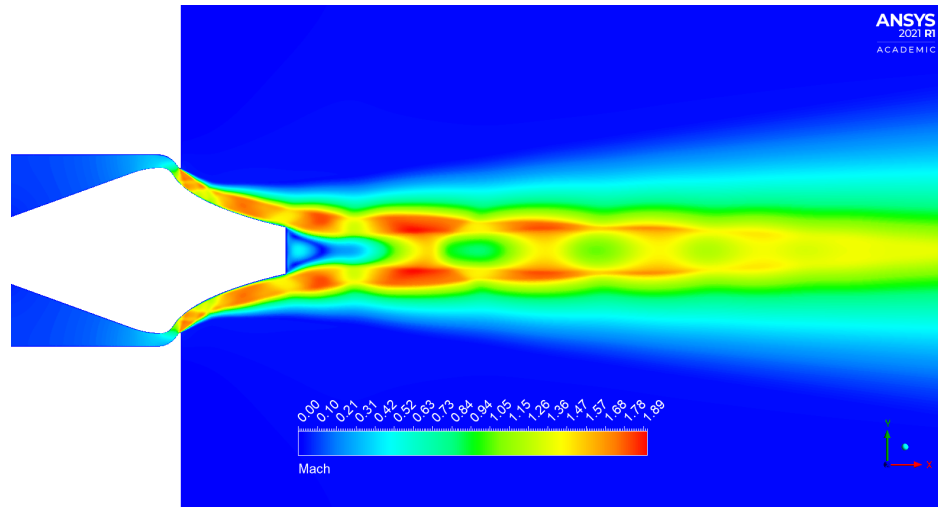
(a) Mach number Contour.



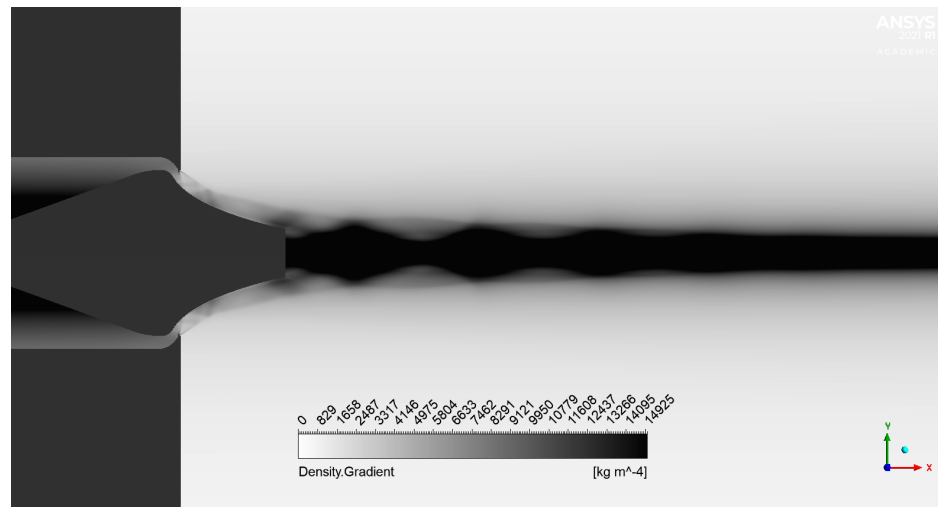
(b) Density gradient contour.

Figure 9.3: Contours of the flow in the conventional bell nozzle under sea-level conditions ($p_{\infty} = 1 \text{ atm}$) (close-up view).

9.2.2 Aerospike nozzle



(a) Mach number Contour.



(b) Density gradient contour.

Figure 9.4: Contours of the flow in the aerospike nozzle under sea-level conditions ($p_{\infty} = 1 \text{ atm}$) (close-up view).

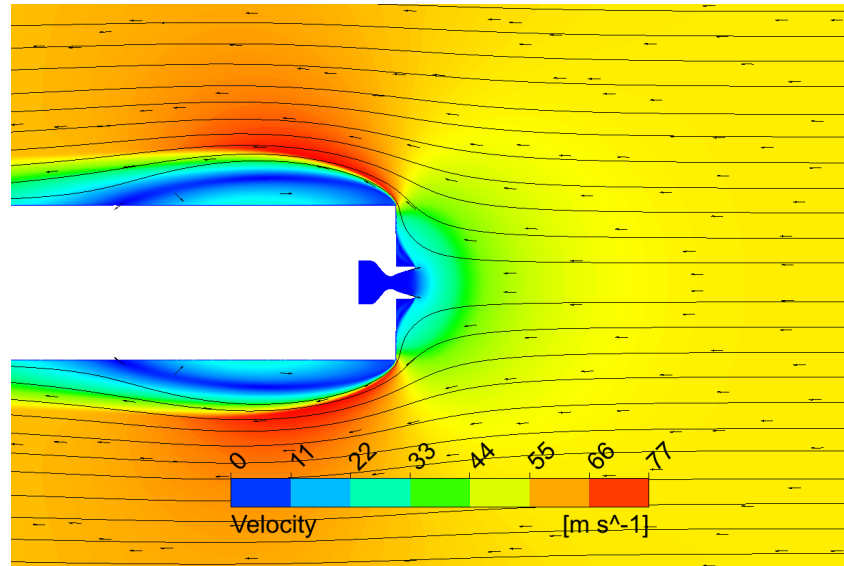
9.3 Case 3: Aerodynamic Descent

For case 3, the nozzle flow is deactivated and only the aerodynamic qualities and performance are to be analyzed. In particular the behaviour of the flow near the wall is of interest. The location of flow separation and the pressure distribution are the main aspects to observe. Contours of velocity magnitude and turbulent kinetic energy (tke) should illustrate this flow behaviour. Pressure measurements at the base and the side are made according to figure 5.4 described in section 5.3. Table ?? summarizes the results of the simulations for case 3.

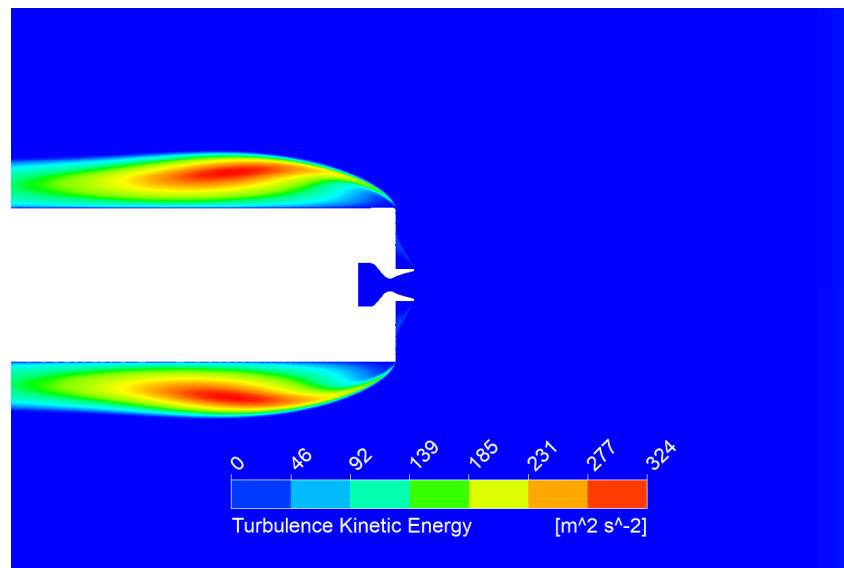
Table 9.3: The aerodynamic parameters of each nozzle configuration for case 3: sea-level free-fall (*the drag values are incomplete and are only valuable as reference).

Parameter	Symbol	Sim. Value		Unit
		Conv. bell	Aerospike	
Freestream st. pressure	p_∞	1,0137	1,0183	bar
Freestream velocity	u_∞	-60	-60	m/s
Side pressure coefficient	C_{ps}	-0,5836	-0,8755	-
Base pressure coefficient	C_{pb}	1,042	0,8531	-
Side velocity	u_s	-76	-78	m/s
Drag force*	D	-16	-17,59	N
Drag coefficient*	C_D	0,9062	0,9154	-

9.3.1 Conventional Bell Nozzle



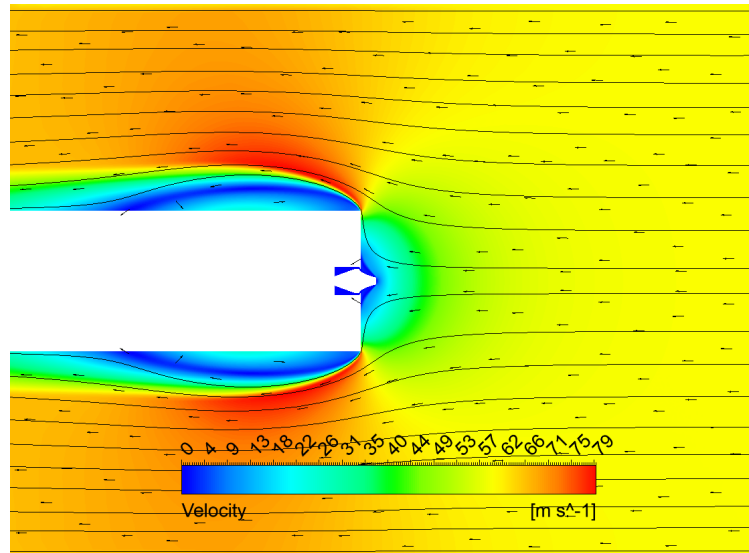
(a) Velocity magnitude contour, vector field and streamlines



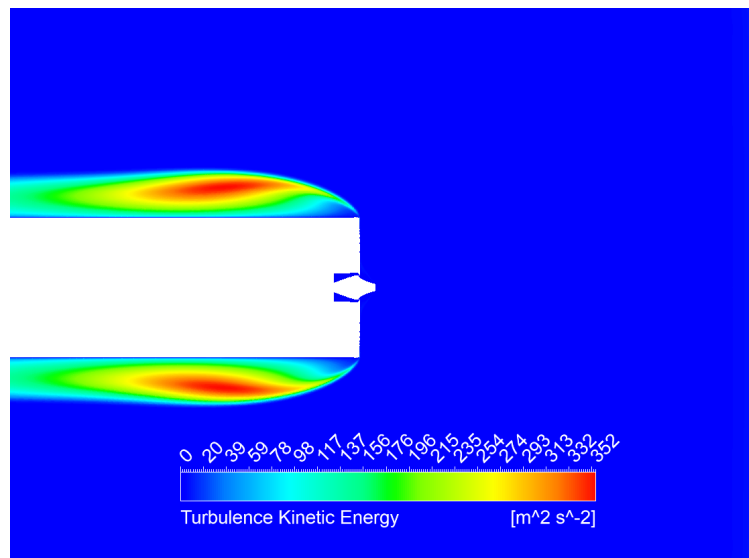
(b) Turbulent kinetic energy contour.

Figure 9.5: Contours of the freestream flow over the booster/bell nozzle configuration under sea-level conditions ($p_{\infty} = 1 \text{ atm}$; $C_D = 0, 906$).

9.3.2 Aerospike nozzle



(a) Velocity magnitude contour, vector field and streamlines



(b) Turbulent kinetic energy contour.

Figure 9.6: Contours of the freestream flow over the booster/aerospike nozzle configuration under sea-level conditions ($p_{\infty} = 1 \text{ atm}$; $C_D = 0, 915$).

9.4 Case 4: Sub-sonic Retro-propulsion

9.4.1 Conventional Bell Nozzle

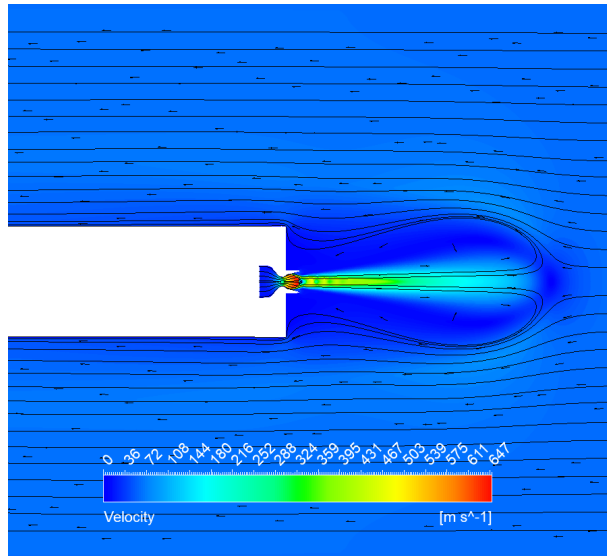
Finally for case 4, both the aerodynamic and nozzle performances are to be evaluated. Attention is placed on the reattachment of the freestream flow on the booster side walls, on the location and topology of the stagnation point, and on the quality of the nozzle flow expansion and its exhaust jet. Table 9.4 shows the aerodynamic parameters and table 9.5 shows the nozzle performance parameters.

Table 9.4: The aerodynamic parameters of each nozzle configuration for case 4: sea-level sub-sonic retro-propulsion (*the drag values are incomplete and are only valuable as reference).

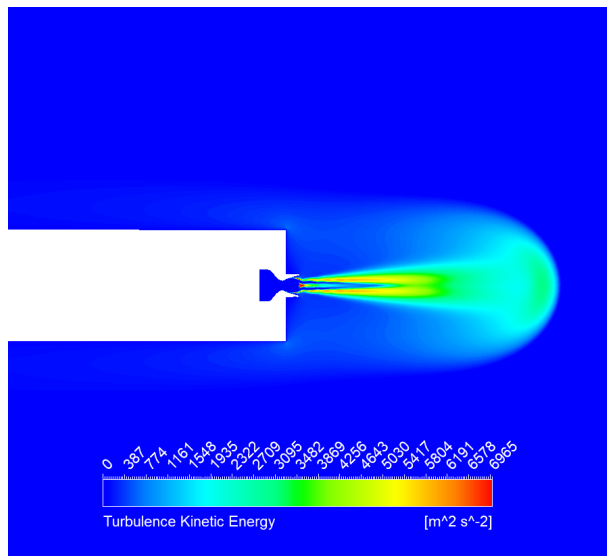
Parameter	Symbol	Sim. Value		Unit
		Conv. bell	Aerospike	
Freestream st. pressure	p_∞	1,0127	1,0199	bar
Freestream velocity	u_∞	-60	-60	m/s
Side pressure coefficient	C_{ps}	0,0098	-0,3398	-
Base pressure coefficient	C_{pb}	0,53	0,2993	-
Side velocity	u_s	-38	-39	m/s
Drag force	D	-9,262	-10,89	N
Aero. drag coefficient	C_D	0,4752	0,5642	-
Momentum flux ratio	f_j/f_∞	0,5283	0,6836	-
Aero. thrust coefficient	C_T	1,143	1,58	-
Distance to stagnation point	l_{st}	259	258	mm

Table 9.5: Simulated nozzle performance values for the conventional bell and the aerospike nozzles in case 4.

Parameter	Symbol	Sim. Value		Unit
		Conv. bell	Aerospike	
Nozzle pressure ratio	p_0/p_a	4,73	4,67	-
Pressure expansion ratio	p_E/p_a	1,147	1,071	-
Axial thrust	F_x	-24,52	-30,42	N
Thrust coefficient	C_F	0,8698	1,13	-
Specific impulse	I_{sp}	38,25	49,17	s

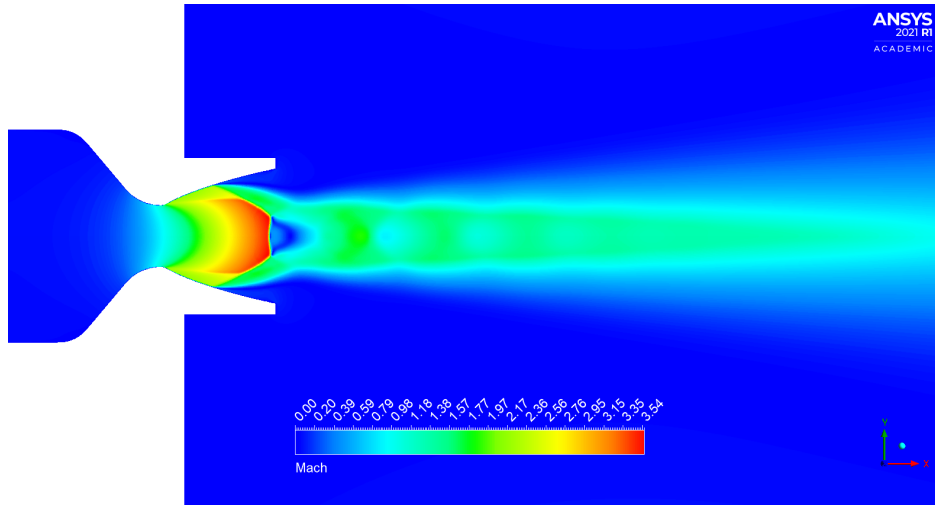


(a) Velocity magnitude contour, vector field and streamlines

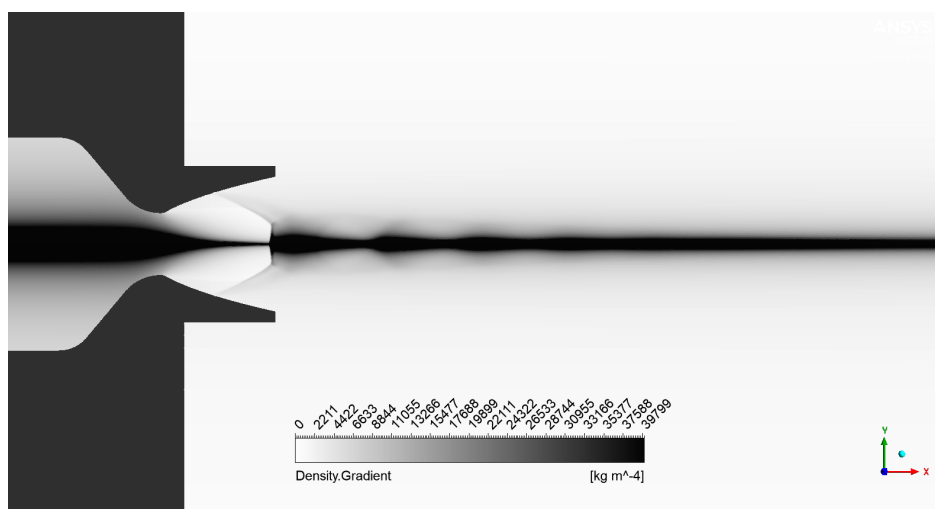


(b) Turbulent kinetic energy contour.

Figure 9.7: Contours of the freestream flow over the booster/bell nozzle configuration under sub-sonic retro-propulsion conditions ($p_\infty = 1$ atm; $C_D = 0,475$; $f_j/f_\infty = 0,53$).



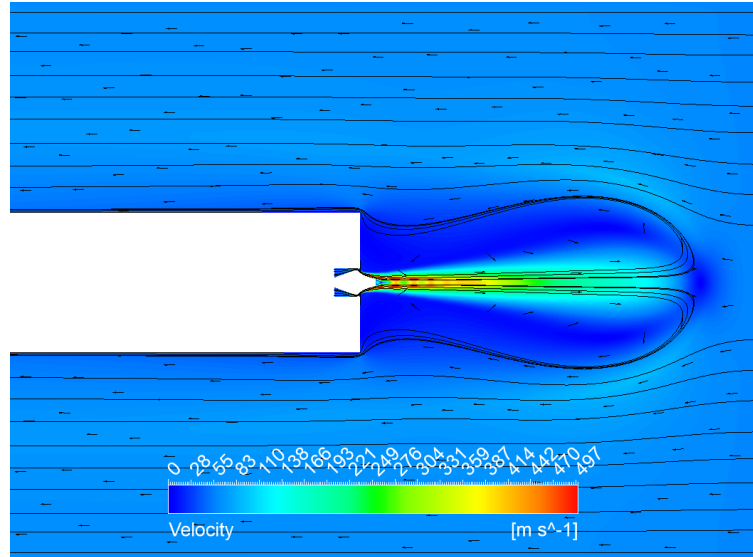
(a) Mach number Contour.



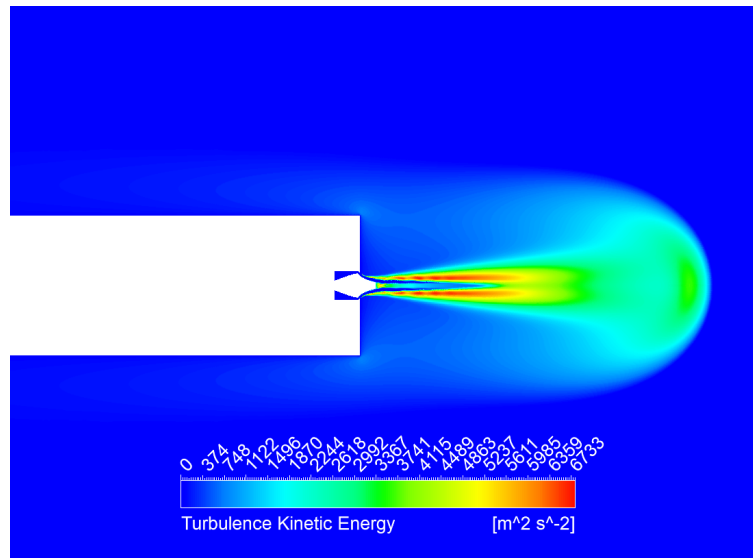
(b) Density gradient contour.

Figure 9.8: Contours of the flow in the conventional bell nozzle under subsonic retro-propulsion conditions ($p_{\infty} = 1 \text{ atm}$; $NPR = 4,73$) (close-up view).

9.4.2 Aerospike nozzle

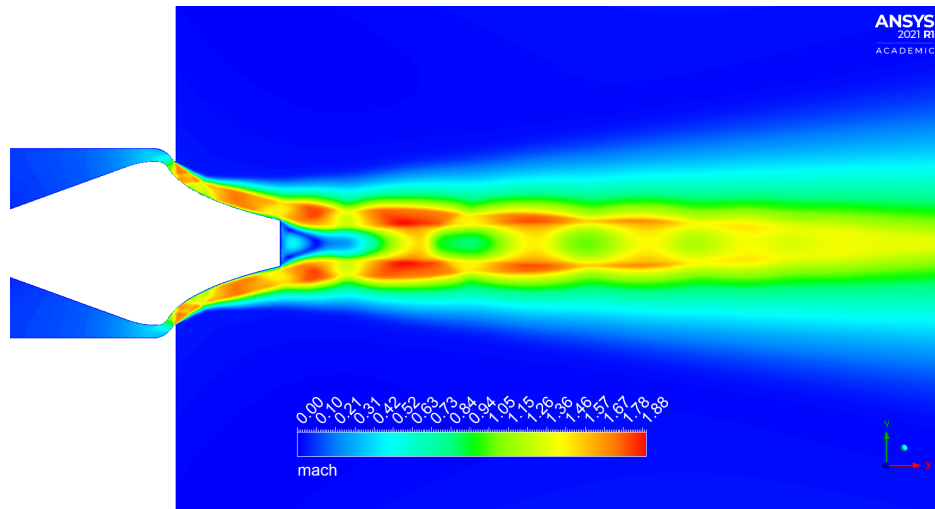


(a) Velocity magnitude contour, vector field and streamlines

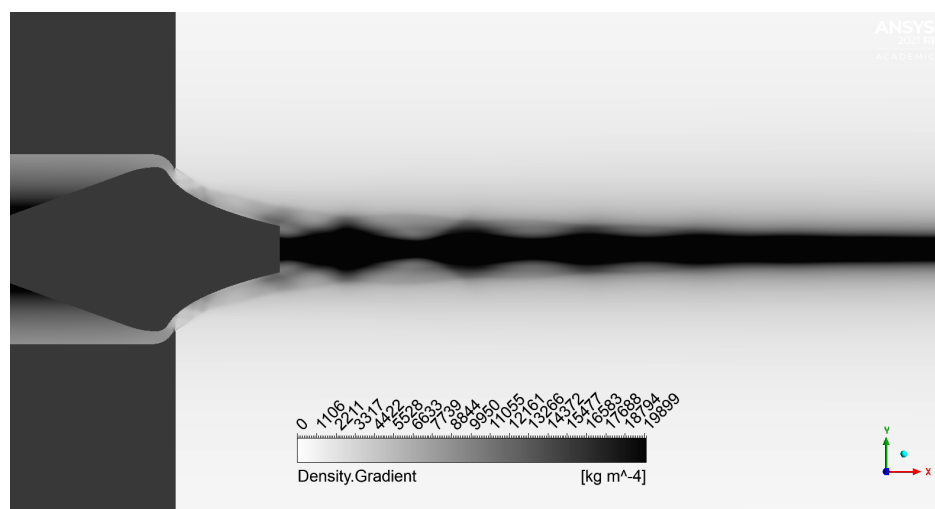


(b) Turbulent kinetic energy contour.

Figure 9.9: Contours of the freestream flow over the booster/aerospike nozzle configuration under sub-sonic retro-propulsion conditions ($p_\infty = 1$ atm; $C_D = 0,564$; $f_j/f_\infty = 0,68$).



(a) Mach number Contour.



(b) Density gradient contour.

Figure 9.10: Contours of the flow in the aerospike nozzle under sub-sonic retro-propulsion conditions ($p_{\infty} = 1 \text{ atm}$; ; $NPR = 4, 67$) (close-up view).

CHAPTER 10

Verification and Preliminary Validation

10.1 Verification

Given the convergence criteria defined in the methodology:

- residuals must sink below 1e-5,
- C_D and f_j values must converge monotonously across more than 100 iterations,

six out of the eight simulations met the criteria. The two simulations that did not were cases 2 and 4 for the conventional bell nozzle. For these two cases, the residuals, the ' C_D ' and the ' f_j ' values tended to converge, only to then begin a cyclical behaviour in a steady pattern every 120 iterations, where the residuals fluctuated about 1,5 orders of magnitude below 1e-2.

A possible explanation for this is that the nozzle flow on these simulations is highly over-expanded and a normal shock-wave emerges inside the nozzle, where a large portion of the flow undergoes dramatic changes in its thermodynamic properties in a very small distance. This normal shock wave is very sensitive to the conditions set at the pressure chamber (mainly from the turbulence intensity), what makes its location and shape hard to predict. Therefore creating an adequate mesh that resolves it to ease the simulation convergence is difficult. To improve these simulations one could prepare a

finer mesh throughout the whole inside of the nozzle to allow the shock wave to be resolved regardless of its emerging position, at a cost of some computational effort. Also, reducing the turbulence intensity in the nozzle inlet boundary may stabilize the flow and ensure a more predictable shape and position of the shock wave.

Comparing analytical and simulation results

For case 1 the nozzle performance simulation results diverged from its analytical counterparts by less than 10%, making these simulations the most trustworthy in this thesis.

For case 2 the aerospike results diverged by less than 7%, but the conventional bell nozzle results diverged dramatically (>50%). This was expected, however, because of the analytical procedure does not consider the presence of the normal shock wave inside the nozzle.

For case 3, the results diverged less than 30%, but were mostly very congruent with the behaviour predicted by the literature. The presence of the different nozzles at the base likely influenced the pressure measurements; this was not considered during the analytical prediction.

Finally for case 4, similar errors to those in case 2 and 3 are observed since case 4 is a combination of these two cases. The predicted pressure at the booster sides was relatively accurate, but the pressure at the base diverged strongly (up to 150%). This proves that the assumptions made were too strong if not completely wrong, and that the flow behaviour in the re-circulation area between the exhaust jet's stagnation point and the booster's base is non-trivial.

In general, the results from the simulations make physical sense and roughly agree with analytical theory and academic literature.

10.2 Preliminary validation

Comparing the results with academic literature and real-life pictures help validate the results qualitatively. The pictures from static burn tests shown in figure 5.2 show an almost identical flow-field topology to figures 9.1 and 9.2 from case 1. However these tests were done as 'hot fire' tests (with combustion) and at bigger scales, so they are not directly comparable.

Data to validate the flow through the over-expanded nozzles from case 2 was not found.

The flowfields in case 3 and 4 resemble the results from Nonaka's research from section 3.1, where during an aerodynamic descent (case 3), a detached freestream flow is observed around the corner at the base of the vehicle. Then, when the nozzle flow is activated, the freestream flow reattaches to the vehicle's side walls. The velocity contours from case 3 and 4 show the exact same qualitative behaviour.

On the quantitative side, the simulations are congruent with Nonaka's observations, where the vehicle's drag and base pressure dramatically decrease, and the side pressure dramatically increases.

Finally, the characteristic values for retro-propulsion are compared: the aerodynamic thrust coefficient C_T , and the momentum flux ratio ' f_j/f_∞ '. The simulations were designed to be comparable with commercial vehicles like the New Shepard and the Falcon 9, and to be compared with Nonaka's 3.1 data. A target ' f_j/f_∞ ' of 0,42 with a 60 m/s counter flow at atmospheric pressure was set. The resulting momentum flux ratios are compared in table 10.1 below. The table shows that the simulations can be appropriately compared to both Nonaka's experiments and to a falcon 9 booster. The simulation momentum flux ratios lie within 27% of the falcon 9 (approximate) value, and within 16% of Nonaka's value.

Table 10.1: A comparison of the momentum flux ratios and aero. thrust coefficients between commercial vehicles, Nonaka's vehicle and the simulation models.

Vehicle	C_T	f_j/f_∞
Bell nozzle Sim.	1,143	0,5283
Aerospike Sim.	1,58	0,6836
Nonaka (case 3)	1,176	0,588
New Shepard	3	1,5
Falcon 9	1,08	0,54

Further validation should come from the experimental campaign by Scarlatella et al. from section 3.4.

CHAPTER 11

Discussion

The discussion can be divided in two parts: the aerodynamic performance, the nozzle performance. The simulations derived, although they can still be further improved in several ways, allow for some initial observations.

11.1 Aerodynamic performance

On the aerodynamic side (see figures 5.3, 5.3, 5.3 and 5.3), the generated contours show the behaviour of the freestream flow in collision with the exhaust jet and around the booster. The nozzle flow/exhaust jet at the stagnation point forms into a water-drop-like shape where it flips direction after a turbulent momentum exchange with the freestream, 'breaking the wind' or cancelling out the freestream's dynamic pressure. A portion of this 'post-stagnation nozzle flow' then accelerates to nearly match the enclosing freestream flow velocity, moving downstream along and attached to the vehicle's lateral walls. The remaining portion of the 'post-stagnation' flow remains trapped in re-circulation in a volume between the freestream and exhaust jet.

At the same time, the freestream smoothly adapts its trajectory over and around the stagnation point. This emerging water-drop like shape upstream from the vehicle arguably creates an ideal aerodynamic (effective) body, dra-

matically reducing the pressure drag, therefore also dramatically reducing the overall aerodynamic drag of the vehicle. This phenomenon was observed by Nonaka (section 3.1) and is confirmed in these simulations. This effect is confirmed by comparing the pressure coefficients on the side and the base of the vehicle from the aerodynamic descent (case 3) with the retro-propulsion (case 4). The base pressure drops by more than 50%, while the side pressure increases by more than 60% for both nozzle configurations. This is characterized by the flow reattachment on the vehicle's lateral walls.

No substantial difference between the aerodynamic performance of both nozzles was observed. One possible difference is that the more compact and aerodynamic shape of the aerospike, allows for a more stable flow that can relieve some mechanical loads on its structure during the aerodynamic descent.

11.2 Nozzle performance

The nozzle designs were validated successfully with the simulations from case 1, where the conventional nozzles achieved 99% of its design thrust, while the aerospike achieved 92%. The discrepancy of 8% in the aerospike nozzle may be due to the thrust calculation method chosen in section 9.4.2, which can be improved. The simulations from case 2 lay a useful reference to compare the results from case 4.

The performance of the aerospike nozzle is substantially better than the conventional bell during a sub-sonic retro-propulsive maneuver (case 4). This statement is certain for these two particular nozzle designs that are optimized to produce 40 N of thrust at an ambient pressure of 0,1067 bar.

In the case of the conventional bell nozzle, the nozzle flow at atmospheric pressure (case 2 and 4) creates the undesired condition of severe over-expansion, with critical detached flow and a normal shock wave that emerges inside the nozzle. The normal shock strongly reduces the exhaust velocity of the nozzle flow, which drastically reduces the performance of the nozzle. This condition also brings flow instabilities, making the flow more unpredictable and increasing chances of high mechanical side-loads that can damage the nozzle.

In the case of the aerospike nozzle, the flow is adapted to the ambient pressure, the flow is attached to the spike walls, and there is no normal shock wave present. This allows the flow to accelerate to higher exhaust velocities

isentropically and in a steady and stable way.

A noteworthy influence of the counter-flow on the nozzle performance is observed during a retro-propulsive maneuver. The consequence of the exhaust jet 'breaking' the counter-flow upstream, is that the effective ambient conditions near the nozzle differ from the freestream ambient conditions. Namely, the effective ambient pressure around the nozzle exit is up to 4% lower than the freestream pressure. This directly influences the performance of an over-expanded nozzle positively, particularly for a non-altitude-adaptive nozzle like the conventional bell, where a thrust increase of up to 3% is observed compared to its static burn under similar conditions. This influence is minimal (<0,03%) on an altitude adaptive nozzle like the aerospike. Regardless of this fact, the aerospike nozzle proves to be better performing.

Comparing the two nozzles under steady-state atmospheric sub-sonic retro-propulsion conditions (case 4) shows that the aerospike performs substantially better than the conventional bell nozzle with a 28,5% higher specific impulse, 24% higher axial thrust, and 30% higher thrust coefficient.

Finally, comparing aerodynamic thrust coefficients, the aerospike nozzle offers a 38% higher value than the conventional bell nozzle. Regardless of this fact, the distance of the stagnation point to the base plate is the same in both configurations. These results may imply that despite the aerospike's higher thrust level, its exhaust jet higher turbulence dissipates its momentum at a higher rate than the conventional bell's counterpart before its collision with the freestream.

CHAPTER 12

Conclusion and Outlook

12.1 Conclusion

A RANS type numerical simulation campaign was carried out to investigate the performance of a conventional bell nozzle and an aerospike nozzle during sub-sonic retro-propulsion, a phenomenon that occurs during the landing burn maneuver of a re-usable launch vehicle (RLV). The emerging flowfields and the resulting aerodynamic behaviour of the vehicle were investigated as well.

These simulation models are comparable to commercial RLV (such as SpaceX's Falcon 9), and although they still offer some room for improvement (mesh refinement studies, convergence stabilisation), they already offer insightful predictions of the aerodynamic and nozzle performances, with aerodynamic results in close agreement (within 8%) with previous experimental campaigns found in literature, and close agreement (within 7%) with analytical approaches for predicting nozzle performance. The simulations, however, are yet to be validated by experimental campaigns.

As control group studies, additional simulations were carried out. Two simulations are done to assess the effect of different ambient pressures (near-vacuum and sea-level) on the performance of both nozzles independently. Validating the nozzle designs first. Then an additional simulation is done to

assess the vehicle's aerodynamic performance before commencing the retro-propulsive maneuver (during free-fall, or aerodynamic descent). The final simulation, sub-sonic retro-propulsion, is the 'experimental group' that overlays both the pressure and counter-flow effects.

The results on the aerodynamic analysis between the aerodynamic descent case and the retro-propulsion case show a dramatic reduction of pressure drag on the vehicle of up to 50% (regardless of the nozzle configuration).

Additionally, a non-trivial positive effect of the counter-flow on the nozzle performance is observed (especially for the conventional nozzle). The counter-flow reduces the local static pressure at the nozzle exit, proportional to the given dynamic pressure component of the freestream ' q_∞ '. This shifts/delays the flow separation point from the nozzle flow further downstream, increasing the performance (I_{sp}) by 4,00% for the conventional bell and 0,14% for the aerospike.

With careful consideration on the point of comparison between the nozzles (both designed to have equal optimal thrust level in near vacuum), the results on the nozzle performance analysis show a clear advantage of the aerospike nozzle over the conventional bell nozzle, with a 28,5% higher specific impulse and a 24% higher thrust level. This suggests, though not yet conclusively, that the aerospike nozzle can substantially improve the efficiency of a landing burn maneuver, potentially reducing the cost of access to space further.

12.2 Outlook

Some proposed future research ideas to build upon this subject are:

- Stabilization and convergence of numerical models for severely over-expanded conventional bell nozzles.
- Performing a mesh refinement study and validation using experimental results to optimize the fidelity of these simulations.
- Expansion of the simulation domain to include the vehicle's complete body and its wake for the proper calculation of the drag force.
- A (similar) comparative study of a conventional bell nozzle designed to avoid severe over-expansion at sea-level with an aerospike nozzle, using another point of comparison than equal optimum thrust at a certain pressure.

- Unsteady RANS simulations of the nozzle flow with increasing pressure over time, recreating the descent during the landing burn.
- Analogous numerical models using the large eddy simulation (LES) method.

Bibliography

- [1] M. Ragab and F. M. Cheatwood, *Launch Vehicle Recovery and Reuse*. [Online]. Available: <https://arc.aiaa.org/doi/abs/10.2514/6.2015-4490>
- [2] H. Jones, “The recent large reduction in space launch cost,” *Texas Tech Libraries*, 2018. [Online]. Available: <https://ttu-ir.tdl.org/handle/2346/74082>
- [3] G. Hagemann, H. Immich, T. Van Nguyen, and G. E. Dumnov, “Advanced Rocket Nozzles,” *Journal of Propulsion and Power*, vol. 14, no. 5, pp. 620–634, 1998. [Online]. Available: <https://doi.org/10.2514/2.5354>
- [4] D. C. Freeman, T. A. Talay, and R. Austin, “Reusable launch vehicle technology programm,” *Acta Astronautica*, vol. 41, no. 11, pp. 777–790, 1997. [Online]. Available: <https://www.sciencedirect.com/science/article/pii/S0094576597001975>
- [5] L. Grush, “Rocket lab successfully brings its rocket back to earth underneath a parachute,” *The Verge*, 2020. [Online]. Available: <https://www.theverge.com/2020/11/19/21578725/rocket-lab-electron-launch-recovery-reusability-parachute-dress-rehearsal>
- [6] SpaceX, “Launches,” *SpaceX*, 2022. [Online]. Available: <https://www.spacex.com/launches/>

- [7] E. Dumont, S. Stappert, T. Ecker, J. Wilken, S. Karl, S. Krummen, and M. Sippel, “Evaluation of Future Ariane Reusable VTOL Booster stages,” in *68th International Astronautical Congress*, September 2017. [Online]. Available: <https://elib.dlr.de/114430/>
- [8] SpaceX, “NROL-76 Launch Webcast,” youtube.com/watch?v=EzQpkQ1etdA, 2017.
- [9] K. Gutsche, A. Marwege, and A. Gülhan, “Similarity and Key Parameters of Retropulsion Assisted Deceleration in Hypersonic Wind Tunnels,” *Journal of Spacecraft and Rockets*, vol. 58, no. 4, pp. 984–996, 2021. [Online]. Available: <https://doi.org/10.2514/1.A34910>
- [10] D. Ghosh and H. Gunasekaran, *Large Eddy Simulation (LES) of Aerospike Nozzle assisted Supersonic Retro-Propulsion (SRP)*. [Online]. Available: <https://arc.aiaa.org/doi/abs/10.2514/6.2021-2489>
- [11] T. Ecker, F. Zilker, E. Dumont, S. Karl, and K. Hannemann, “Aero-thermal Analysis of Reusable Launcher Systems during Retro-Propulsion Reentry and Landing,” 05 2018.
- [12] E. O. Daso, V. E. Pritchett, T.-S. Wang, D. K. Ota, I. M. Blankson, and A. H. Auslender, “Dynamics of Shock Dispersion and Interactions in Supersonic Freestreams with Counterflowing Jets,” *AIAA Journal*, vol. 47, no. 6, pp. 1313–1326, 2009. [Online]. Available: <https://doi.org/10.2514/1.30084>
- [13] S. Nonaka, H. Nishida, H. Kato, H. Oogawa, and Y. Inatani, “Vertical Landing Aerodynamics of Reusable Rocket Vehicle,” *Transactions of the japan society for aeronautical and space sciences, aerospace technology japan*, vol. 10, pp. 1–4, 2012.
- [14] B. Origin, “New Shepard Successfully Flies 8 NASA Research Technology Payloads to Space,” <https://www.blueorigin.com/news/new-shepard-successfully-flies-8-nasa-research-and-technology-payloads-to-space>, 2019.
- [15] D. Huzel and D. Huang, *Design of Thrust Chambers and Other Combustion Devices*, ch. 4, pp. 67–134. [Online]. Available: <https://arc.aiaa.org/doi/abs/10.2514/5.9781600866197.0067.0134>

- [16] N. Taylor, J. Steelant, and R. Bond, “Experimental comparison of Dual Bell and Expansion Deflection Nozzles,” 07 2011.
- [17] “Rocket nozzle design.” [Online]. Available: <https://www.grc.nasa.gov/WWW/k-12/rocket/nozzle.html>
- [18] C. Bach, “Systemanalyse und Prototypenentwicklung einer durch Fluid-injektion induzierten Schubvektorsteuerung für Aerospike-Triebwerke,” Ph.D. dissertation, Technische Universitaet Dresden, 2019.
- [19] N. V. Taylor, C. M. Hemsell, J. Macfarlane, R. Osborne, R. Varvill, A. Bond, and S. Feast, “Experimental investigation of the evacuation effect in expansion deflection nozzles,” *Acta Astronautica*, vol. 66, no. 3, pp. 550–562, Feb. 2010.
- [20] G. Scarlatella, “Cold-flow tests on advanced nozzle concepts in subsonic retro-flows: development of test-bench,” *AIDAA*, 2021.
- [21] J. Anderson, *Basic Philosophy of CFD*. Berlin, Heidelberg: Springer Berlin Heidelberg, 2009, pp. 3–14. [Online]. Available: https://doi.org/10.1007/978-3-540-85056-4_1
- [22] E. Dick, *Introduction to Finite Volume Methods in Computational Fluid Dynamics*. Berlin, Heidelberg: Springer Berlin Heidelberg, 2009, pp. 275–301. [Online]. Available: https://doi.org/10.1007/978-3-540-85056-4_11
- [23] R. Bhaskaran, “A hands-on introduction to engineering simulations,” January 2021.
- [24] J. Vierendeels and J. Degroote, *Aspects of CFD Computations with Commercial Packages*. Berlin, Heidelberg: Springer Berlin Heidelberg, 2009, pp. 305–328. [Online]. Available: https://doi.org/10.1007/978-3-540-85056-4_12
- [25] W. L. Oberkampf and T. G. Trucano, “Verification and validation in computational fluid dynamics,” *Progress in Aerospace Sciences*, vol. 38, no. 3, pp. 209–272, 2002. [Online]. Available: <https://www.sciencedirect.com/science/article/pii/S0376042102000052>
- [26] ANSYS, “Ansys fluent meshing user’s guide,” January 2016.

- [27] F. Stern, R. V. Wilson, H. W. Coleman, and E. G. Paterson, “Verification and validation of cfd simulations,” Iowa Institute of Hydraulic Research Iowa City, Tech. Rep., 1999.
- [28] S. T. Committee, “Terminology for model credibility,” *Simulation*, vol. 32, no. 3, pp. 103–104, 1979. [Online]. Available: <https://doi.org/10.1177/003754977903200304>
- [29] Y. Zhao, H. D. Akolekar, J. Weatheritt, V. Michelassi, and R. D. Sandberg, “RANS turbulence model development using CFD-driven machine learning,” *Journal of Computational Physics*, vol. 411, p. 109413, 2020. [Online]. Available: <https://www.sciencedirect.com/science/article/pii/S002199912030187X>
- [30] J. Sodja, “Turbulence models in CFD,” *University of Ljubljana*, pp. 1–18, 2007.
- [31] B. Origin, “Blue Origin NS-14 Launch! (Rocket and Capsule Landing),” <https://www.youtube.com/watch?v=laLnop6LeFt=557s,> 2022.
- [32] SpaceX, “Falcon Heavy Test Flight ,,” <https://www.youtube.com/watch?v=wbSwFU6tY1c,> 2018.
- [33] SpaceX., “Falcon 9,” <https://www.spacex.com/vehicles/falcon-9/>, 2022.
- [34] B. Origin, “New shepard,” <https://www.blueorigin.com/new-shepard/,,> 2022.
- [35] C. E. Cordell, I. G. Clark, and R. D. Braun, “CFD verification of supersonic retropropulsion for a central and peripheral configuration,” in *2011 Aerospace Conference*, 2011, pp. 1–22.
- [36] D. G. Schauerhamer, K. A. Zarchi, W. L. Kleb, and K. T. Edquist, “Supersonic retropropulsion CFD validation with Ames Unitary Plan Wind Tunnel test data,” in *2013 IEEE Aerospace Conference*, 2013, pp. 1–14.
- [37] F. Rossberg, “Set-up and commisioning of a counter-flow nozzle experiment in the vacuum wind channel,” Ph.D. dissertation, Technische Universitaet Dresden, 2021.
- [38] M. Leonhardsberger, “Studienarbeit,” Ph.D. dissertation, Technische Universitaet Dresden, 201x.

- [39] D. Surek and S. Stempin, *Stationäre inkompressible Strömung; Hydrodynamik*. Wiesbaden: Springer Fachmedien Wiesbaden, 2014, pp. 43–159. [Online]. Available: [https://doi.org/10.1007/978-3-658-06062-6₃](https://doi.org/10.1007/978-3-658-06062-6_3)
- [40] F. Jorde, “Diplomarbeit,” Ph.D. dissertation, Technische Universitaet Dresden, 2018.
- [41] G. P. Sutton and O. Biblarz, *ISENTROPIC flow through nozzles*, ch. 3, pp. 52–74. [Online]. Available: <https://www.wiley.com/en-us/Rocket+Propulsion+Elements%2C+9th+Edition-p-9781118753651description-section>
- [42] A. Engineering, “Test firing of 3d-printed rocket engine,” <https://www.youtube.com/watch?v=-cZn2mnq0yY>, 2021.
- [43] P. Aerospace, “Pangea aerospace engine hot run,” <https://www.youtube.com/watch?v=CombVB48ziY>, 2021.
- [44] J. Anderson, *Fundamentals of Aerodynamics*. McGraw-Hill Education, 2016. [Online]. Available: <https://books.google.pt/books?id=D1ZojgEACAAJ>
- [45] C. Tapia, “spacetoolbox,” <https://github.com/carlostapiaman/spacetoolbox>, 2021.
- [46] M. Vernacchia, “Spike contour algorithm,” <https://github.com/mvernacc/aerospike-nozzle-design-gui>, 2013.
- [47] aerorocket.com, “Thickness of a normal shock,” <http://www.aerorocket.com/Nozzle/Validate/Tshock/Shock.html>.
- [48] A. Wimshurst, “Inflation layers calculator,” <https://www.fluidmechanics101.com/pages/tools.html>, 2022.